Politecnico di Torino

Corso di Laurea Magistrale
In Ingegneria per l'Ambiente e il Territorio

A.A. 2023/2024
Sessione di Laurea Marzo 2024

APPLICATION OF A SATELLITE-BASED SOIL MOISTURE RETRIEVAL TECHNIQUE TO IRRIGATED AREAS IN PIEMONTE

Relatori:
Prof. Stefania Tamea
Dr. Matteo Rolle

Candidato:
Mario Chalouhy

ABSTRACT

Water is an indispensable resource for human activities and agriculture. Its scarcity has severe consequences, including impacts on hygiene, sanitation, nutrition, and food security. Access to clean drinking water is a basic human right, yet it remains a challenge in many parts of the world. This calls for a paradigm shift in our approach to water management, which includes adopting a proactive approach that goes beyond our present needs and aims to safeguard the resource for the well-being of the environment and future generations.

As numerous studies have already highlighted, all solutions towards better management begin with the same step: achieving a good quantitative knowledge, primarily through significant technological improvement. This is fundamental as it would enable an accurate assessment of the current situation in addition to tracking its evolution and evaluating any proposed solutions in the future. Given the complexity of the water cycle and the large scale over which it occurs, in-situ point measurements have been shown to be quite insufficient in addressing this issue. In contrast, the large scales provided by radars and satellites has led researchers to regard them as sources of great potential. Given the fact that irrigation practices are estimated to be responsible for more than 70% of global water withdrawals, using these large-scale studies in order to estimate irrigation quantities, in particular, has proven to be of critical importance.

In Europe, the large majority of such studies rely on the Sentinel-1 mission provided by the Copernicus Program thanks to its open access. The loss of one of the two twin radars, Sentinel-1B, at the end of 2021, doubled the mission's revisit period and, thus, greatly impacted studies relying on this data. Unfortunately, all the following efforts to make up for this loss, namely in the attempts to launch Sentinel 1-C and Sentinel 1-D, have faced either delays or failures. In this context, the first part of this study includes an investigative analysis of radar missions that could potentially be used, as separate alternatives or complementary sources to Sentinel-1, for radar data.

In addition to this, this study attempts to build on the latest research on the topic of obtaining irrigation estimates based on the inversion of soil moisture data obtained from radar data by relying on adapted versions of two main algorithms: SM2Rain and RT1. SM2Rain is an algorithm originally developed for the retrieval of rainfall estimates from soil moisture data. RT1, on the other hand, is a new radiative-transfer modeling framework for the retrieval of soil moisture estimates, which originally relied on scatterometer data. Therefore, this study also presents a regional-scale, high-resolution (∼1 km) irrigation data set obtained using the above-mentioned methods.

The study area consists of 73km^2 of agricultural areas in Piedmont, Italy, falling within the Canavese area, between Chivasso and Caluso. The time period considered spans over the years of 2020 to 2022. Radar data was obtained from the Sentinel-1 mission through the Copernicus website. Meteorological data was obtained from ARPA Piemonte, specifically from the Caluso station, which is centered within our area of interest. The analysis also made use of other sources, such as ERA5-Land hourly data from 1950 to present for Leaf Area Index (LAI) and benchmark soil moisture data, in addition to irrigation calendar data specific to the considered agricultural areas.

ACKNOWLEDGEMENTS

I would like to express my deepest appreciation to my thesis supervisor, Dr. Stefania Tamea, for trusting me with the opportunity to work on this research, and who, along with my co-supervisor Dr. Matteo Rolle, offered their valuable time and expertise and provided continuous guidance and feedback throughout this journey.

I am thankful to the academic and administrative staff members at Politecnico di Torino for their personal commitment to foster an environment that encourages learning, growth, and teamwork. My sincere gratitude goes to all the Professors that had me as a student; their dedication and genuine passion to teaching, shown in their unwavering efforts to provide a thorough understanding of the material and in their patience and commitment to answering my numerous questions and doubts, have been invaluable for my learning path and left a lasting impact on me personally.

I'd also like to acknowledge the colleagues and friends who spent these last few years with me for making this journey a truly special one, and Joey for making life abroad feel like home. Lastly, I'd like to mention my brothers, Hatem and Chady, for their unconditional support and encouragement before, during, and after this journey, and without whom none of it would have been possible.

TABLE OF CONTENTS

Abstract ii
Acknowledgements iii
Table of Contents iv
List of Tables v
List of Figures vi
List of Abbreviations vii
1. Introduction 1
2. Data Sources and Analysis 5
2.1. Radar Data 1: Sentinel-1 Data 5
2.2. Radar Data 2: Alternatives to Sentinel-1 6
2.3. Soil Moisture Data 9
2.4. Potential Evapotranspiration Data 9
2.5. Meteorological Data 9
2.6. Reanalysis Data 10
2.7. Benchmark Irrigation Data 11
3. Methodology 13
3.1. First-order Radiative Transfer (RT1) Model 13
3.1.1. Theoretical Background 13
3.1.2. Implementation of RT1 Algorithm 18
3.2. The SM-based Inversion Approach 26
3.2.1. Theoretical Background 26
3.2.2. Implementation of SM2Rain Algorithm 34
4. Results and Discussion 40
4.1. RT1 40
4.1.1. Correlation Between N and Baseline Soil Moisture 40
4.1.2. Comparison of Scaling Methods from N to SM 43
4.1.3. Analysis of SM Estimates using Baseline Irrigation Data 45
4.2. SM-Based Inversion 46
4.2.1. Fitting Results 46
4.2.2. Irrigation Estimates 47
4.3. Limitations 48
5. Conclusions 50

Appendix A 52
References 56

LIST OF TABLES

Table 1 - List of alternative SARs that were investigated 7
Table 2 - Results of investigation into alternative SAR's 8
Table 3 - Reanalysis parameters obtained from C3S (2024) 11
Table 4 - Statistics for irrigation calendar data 12
Table 5 - Summary of the model parameters' specifications 23
Table 6 - Coarse-resolution radar sensors/missions for soil moisture estimation (evaluated by Brocca et al., 2018) 30
Table 7 - Summary of alternative SM datasets considered in the SM-inversion approach 35
Table 8 - Data template before aggregation 36
Table 9 - Data template after aggregation 36
Table 10 - Aggregated data template prior to fitting 37
Table 11 - Summary of model calibration attempts done in SM-based inversion algorithm 39
Table 12 - Summary statistics for swvl1 and the four SM datasets 43
Table 13 - Summary of weights and areas obtained from irrigation calendars 45
Table 14 - Fitting results for SM-based inversion algorithm 46
Table 15 - Statistics for a, b, and Z* - fitting attempt 1 53
Table 16 - Statistics for a, b, and Z* - fitting attempt 2 53
Table 17 - Statistics for a, b, and Z* - fitting attempt 3 54
Table 18 - Statistics for a, b, and Z* - fitting attempt 4 54
Table 19 - Statistics for a, b, Z*, and T - fitting attempt 5 54
Table 20 - Statistics for a, b, Z*, and T - fitting attempt 6 54
Table 21 - Statistics for a, b, Z*, and T - fitting attempt 7 55
Table 22 - Statistics for a, b, Z*, and T - fitting attempt 8 55

LIST OF FIGURES

Figure 1 - Location of considered study area....4
Figure 2 - Map showing location of chosen station for meteorological data (using QGIS and OpenStreetMap)....10
Figure 3 – Map showing irrigation calendar data obtained from Consortium of Caluso Canal (using QGIS and OpenStreetMap) 12
Figure 4 - Scheme displaying the different contributions to backscatter radiation received by a SAR (Quast et al., 2016)....14
Figure 5 - Alternative scheme showing individual contributions to backscatter signal (Quast et al., 2019) 15
Figure 6 - Generated target grid, with 1 km spatial resolution, for the considered study area 19
Figure 7 - Map displaying boundaries of sample SAR images that only partially overlap AOI (using QGIS and OpenStreetMap) 21
Figure 8 - Summary of fitting procedure adopted in Brocca et al., 2018 (source: Brocca et al., 2018)....32
Figure 9 - Summary of fitting procedure adopted in Dari et al., 2020 (source: Dari et al., 2020)....33
Figure 10 - Summary of iterative fitting procedure adopted in Dari et al., 2023 (source: Dari et al., 2023) 33
Figure 11 - PET (obtained using Hargreaves) and Precipitation (obtained from Caluso meteo-station) timeseries....36
Figure 12 - Summary of iterative fitting procedure adopted in this study 38
Figure 13 - Density plot of Pearson correlation for RT1 results – per period....40
Figure 14 - Spatial distribution of Pearson correlation for RT1 results 41
Figure 15 - Density plot of Pearson correlation for RT1 results – per period....41
Figure 16 - Spatial distribution of Pearson correlation for RT1 results - per period 42
Figure 17 – Map showing the number of SAR images intersecting the agricultural areas (using QGIS and OpenStreetMap) 43
Figure 18 - Timeseries of average SM values for two SM estimate alternatives and baseline SM 44
Figure 19 - Plots of SM, P, and p(I) - Cell 1....45
Figure 20 - Plots of SM, P, and p(I) - Cell 2....46
Figure 21 - Timeseries for irrigation and precipitation, averaged across all cells in the target grid 48
Figure 22 - Comparison of Pearson correlation density plots for RT1 results before and after resampling – 2020-2021 52
Figure 23 - Comparison of Pearson correlation density plots for RT1 results before and after resampling – 2022 52
Figure 24 - Timeseries of average resampled SM values for two SM estimate alternatives and baseline SM....53

LIST OF ABBREVIATIONS

AMSR2	Advanced Microwave Scanning Radiometer 2
ARPA	Agenzia Regionale per la Protezione Ambientale
ASCAT	Advanced SCATterometer
BRDF	Bidirectional Reflectance Distribution Function
C3S	Copernicus Climate Change Service
CDS	Climate Data Store
CRS	Coordinate Reference System
CSAR	C-Band Sensor
DA	Data Assimilation
DISPATCH	DISaggregation based on Physical And Theoretical scale CHange
DOW	Day of Week
ECMWF	European Centre for Medium-Range Weather Forecasts
EEA	European Environment Agency
ESA	European Space Agency
ET	Evapotranspiration
FAO	Food and Agriculture Organization
GLEAM	Global Land Evaporation Amsterdam Model
GRDH	Ground- Range-Detected at High resolution
HG	Henyey-Greenstein
LAI	Leaf Area Index
PBIAS	Percent Bias
PET	Potential Evapotranspiration
PDF	Probability Density Function
RMSE	Root Mean Square Error
RT1	First-order Radiative Transfer model
RTE	Radiative Transfer Equation
SAR	Synthetic Aperture Radar
SM	Soil Moisture
SMAP	Soil Moisture Active Passive
SMOS	Soil Moisture and Ocean Salinity
swvl1	Volumetric Soil Water Level 1 (0-7 cm)
UNESCO	United Nations Educational, Scientific and Cultural Organization
UTM32	Universal Transverse Mercator Zone 32 North
VV	Vertical-Vertical polarization
WGS84	World Geodetic System 1984

1. INTRODUCTION

Water has been an indispensable resource throughout human history. In ancient times, human settlements were intricately tied to the availability of water sources, such as lakes and rivers. Civilizations, cities, and villages emerged near these water sources, forming the backbone of their social and economic activities. Technological progress, including the development of extensive water networks, the construction of dams, and the establishment of wells and other critical infrastructure, enabled societies to harness the diverse water sources available to them. These innovations allowed cities and communities to expand and flourish. As a result, urbanization, agriculture, and industries thrived, driving progress and prosperity. However, as our reliance on these engineered water systems grew, so did the challenge of overexploitation. Driven by population growth, industrialization, and shifting consumption patterns, the demand on water resources has reached unprecedented levels.

Access to clean drinking water is a basic human right, yet it remains a challenge in many parts of the world. According to the United Nations Educational, Scientific and Cultural Organization (UNESCO, 2021), nowadays, it is estimated that 50% of malnutrition is directly caused by lack of proper water, sanitation, and hygiene. Moreover, water is a cornerstone of food security, as it is required for crop cultivation and livestock farming. The ecological consequences of over-extraction are evident in the depletion of aquifers, the alteration of natural flow patterns in rivers, and the degradation of aquatic habitats. Furthermore, due to the complex nature of Earth's environment, these alterations often lead to positive reinforcement effects, in the sense that they weaken the resilience of water systems, making them vulnerable and thus unable to cope with the uncertainties brought about by climate change, thus exacerbating issues of water scarcity and quality (Nian et al., 2014, Mutiga et al., 2010). Despite the numerous uses for water, agriculture seems to be, by far, the most influential. In fact, according to UNESCO's 2021 World Water Development Report, agriculture, alone, is responsible for 69% of global freshwater use. This is further confirmed by the European Environment Agency (EEA, 2023), which states that agriculture accounts for around 40 % of the total water used per year in Europe, making it the top contributor to water use. In fact, irrigation practices are estimated to be responsible for more than 70% of global water withdrawals (Foley et al., 2011; Dorigo et al., 2021). In addition to that, future projections estimate that the issue of water scarcity is only expected to get worse. According to Wang et al. (2014), climate change is expected to cause further increase in global water demand.

This calls for a paradigm shift in our approach to water management. To address this challenge, it is necessary to adopt a proactive approach that not only considers present needs but also safeguards the resource for the well-being of the environment and future generations. One of the main barriers to the development of suitable management and adaptation actions and strategies is the lack of proper monitoring, as highlighted by several scientific articles. Two notable examples are Knüppe et al. (2016) that discussed the importance and urgency of adequate monitoring and Lawford et al. (2013) that explained the essential role of integrating both in-situ and satellite data in achieving this goal. In this context, given that good data is the foundation of analytics, improving the quantity and quality of monitoring data is fundamental in order to perform more robust analyses, achieve more definitive results with higher certainty, guide decision-making, and evaluate the results of previous decisions.

The role of remote sensing in achieving this goal has been huge, as demonstrated by Boori et al. (2021). This is mainly due to the broad spatial scale offered by radars and satellites, compared to the traditional in-situ measurement methods, which mainly rely on localized, point measurements. It offers a hefty amount of data with consistency and reliability, two essential factors that are often lacking in irrigation

monitoring data (Alexandridis et al., 2013). Remote sensing, then, is very helpful in giving a more comprehensive overview about environmental phenomena. The importance of this technology is only expected to increase in magnitude as remote-sensing data becomes more accessible (Lechner et al., 2020), as better integration of remote sensing with in-situ data is developed (Lawley et al., 2016), and as remote-sensing instruments achieve better spatial and temporal coverage.

A significant amount of effort to develop methods and procedures that make use of remote sensing data to tackle this issue has already been made and published in the literature. As described by Dari et el. (2022), the issue of irrigation monitoring can be split into two main parts: identification (of irrigation events) and quantification (of the water quantities involved in the process). The task of identification has seen notable progress; the quantification task, on the other hand, has proven to be relatively more challenging, with the first irrigation quantification method based on the inversion of soil moisture estimates (also known as SM-based inversion approach) being proposed by Brocca et al. (2018). While the method's feasibility was demonstrated in that study using several soil moisture datasets, its reliance on coarse-resolution soil moisture data was acknowledged as a major limitation. In another notable study, Jalilvand et al. (2019) demonstrated the significant role of the evapotranspiration component, specifically in the case of semi-arid regions. Dari et al. (2020) built on that by adopting the guidelines of the Food and Agriculture Organization (FAO) to better represent the evapotranspiration component within the SM-inversion approach and adopted downscaled soil moisture inputs to improve overall model precision. Alternatives to the SM-approach have also been developed, namely the SM-delta (soil-moisture-delta) approach, first proposed by Zaussinger et al. (2019). This method quantifies the water volumes involved in irrigation as the difference between modeled soil moisture and soil moisture estimates obtained from satellite data. Zappa et al. (2021) later suggested some improvements to the SM-delta method by introducing to it terms that account for evapotranspiration and drainage fluxes. In addition to the above, several studies have shown that data assimilation (DA) techniques can be applied on soil moisture estimates obtained from remote sensing data in order to improve models in irrigation quantification studies (Ozdogan et. al., 2010; Lawston et al., 2015; Nie et al., 2018). Some studies proposed the use of DA to integrate retrieval remote sensing products into irrigation quantification models, such as Lawston et al. (2017), Jalilvand et al. (2021), and Abolafia-Rosenzweig et al. (2019). Others, namely De Lannoy and Reichle (2016a, b), Lievens et al. (2017a, b), and Modanesi et al. (2022), proposed the use of DA to directly integrate level-1 observations (such as radar-backscatter) instead of retrievals. Finally, the latest effort to mention is the study of Dari et al. (2023). In that study, they adopted a slightly modified approach to the SM-based inversion method, with the introduction of a first-order Radiative Transfer model (also known as RT1) (Quast & Wagner, 2016; Quast et al., 2019) to calculate soil moisture estimates, as opposed to relying on the downscaling of coarse soil moisture products. This allowed them to obtain, for the first time, regional-scale and high-resolution irrigation water data sets from satellite observations. This proposed alternative serves as a great example of the growing role of remote sensing in tackling important issues related to climate change. Even though the RT1 approach initially relied on scatterometer, the feasibility of adapting the approach to make use of Sentinel-1 backscatter was validated in the study of Quast et al. (2023), which also included a thorough analysis and discussion of the limitations and implications of doing so.

Despite the potential provided by radars and satellites, however, one prominent issue that remains to be tackled, especially with radar data, is data availability. The large majority of studies dealing with radar data rely on the Sentinel-1 mission due to the open-access provided by the Copernicus Programme. The loss of one of the two twin radars, Sentinel-1B, at the end of 2021, doubled the mission's revisit period from 6 days to 12 days and, thus, greatly impacted studies relying on it for radar data. Unfortunately, all the following efforts to make up for this loss, namely in the attempts to launch Sentinel 1-C and Sentinel 1-D, have faced either delays or failures. In this context, the first part of this study contains a detailed

investigative analysis of alternative radar missions, and the main obstacles and opportunities currently encountered with regards to the availability and accessibility of radar data.

This is followed by an attempt to adopt adapted versions of the RT1 algorithm (Quast et al., 2023) to generate soil moisture estimates and the SM-based inversion algorithm (Dari et al., 2023) to obtain a regional-scale, high-resolution (~1 km) data set of irrigation estimates.

The considered study area consists of 73 km^2 of agricultural areas in Piedmont, Italy. More specifically the areas fall within the Canavese area, between Chivasso and Caluso, as shown in Figure 1 below. The areas are intensively irrigated, mainly in the summer period between June and September. They mostly rely on the Caluso Canal, which spreads over several kilometers and plays a crucial role for agriculture in the area. It has an average rainfall of around 630 mm/year.

Considering the World Geodetic System 1984 (WGS84) coordinate reference system (CRS), the area has a bounding box that extends over 0.25° of latitude, ranging from 7.74 to 7.99 °E, and 0.19° of longitude, ranging from 45.19 to 45.38 °N. Considering the equivalent projected coordinates onto the Universal Transverse Mercator Zone 32 North (UTM32), it can be deduced that the area's bounding box has an approximate area of 378 km^2 (19.625 x 19.250 km).

Figure 1 - Location of considered study area

The time period considered spans from the beginning of 2020 until the end of 2022. The period of 2020-2021 was used for model fitting. The fitted models were then used to produce irrigation estimates for the year 2022. Soil moisture data was calculated, via a slightly modified version of the most recent RT1 algorithm proposed in the study of Quast et al., (2023), using Sentinel-1 images obtained from the website of the European Space Agency (ESA) and Leaf Area Index (LAI) data. The LAI data, in addition to baseline soil moisture data, namely Volumetric Soil Water Level 1 (swvl1 – 0-7 cm), was obtained from the website of the Climate Change Service. Temperature and precipitation data were obtained from the website of the Agenzia Regionale per la Protezione Ambientale (ARPA) Piemonte. Benchmark irrigation data was obtained from Il Consorzio del Canale Demaniale di Caluso (The Consortium of the Caluso State Canal).

The paper is organized as follows. The input data, required to run and verify the RT1 and SM-based inversion algorithms, is described in Section 2. The adopted methodology is described in Section 3 including details concerning the theoretical background and the actual implementation of each of the two algorithms. Results are displayed and discussed in Section 4. Finally, concluding remarks are discussed in Section 5.

2. DATA SOURCES AND ANALYSIS

This section presents details about the main data inputs for the RT1 and the SM-based inversion algorithms. The data used in this study can be split into two main categories: acquired data and computed data.

Acquired data consists of the data variables that were obtained as raw data from an external source, and possibly underwent some processing steps such as error corrections and spatial and/or temporal resampling. This includes radar data (Section 2.1), temperature and precipitation data (Section 2.5), benchmark irrigation data (Section 2.7), in addition to LAI and baseline soil moisture (swvl1) datasets (Section 2.6).

Computed data consists of the data variables generated, within the study and from other independent variables, through the use of specific formulas or algorithms. This includes soil moisture (Section 2.3) and potential evapotranspiration (Section 2.4). They are included in this section, along with the acquired data, because they, too, were used as inputs to obtain the final output, which is irrigation estimates.

In addition to that, despite the inability to acquire alternative radar data to those from Sentinel-1, an informative summary of the investigation done into alternative missions and the main findings from it are included in Section 2.2.

2.1. Radar Data 1: Sentinel-1 Data

The crucial role of remote sensing, discussed in the previous section, in quantifying agricultural water usage relies, first and foremost, on the remotely-sensed data itself. Specialized instruments like Synthetic Aperture Radars (SARs), which are known for their ability to penetrate cloud cover and provide all-weather, day-and-night imaging capabilities, are responsible for generating this data. The significance of collected data, however, can be compared to Schrödinger's cat or the tree that falls in a lonely forest; it only gains impact or significance when properly observed. In other words, the true potential of radar data is unlocked, not when it’s collected, but when it’s made available so that it can be meticulously analyzed, thereby yielding invaluable insights that can inform effective actions and policies in the ongoing battle against Climate Change.

The Sentinel-1 mission, an integral component of the European Space Agency's (ESA) Copernicus program, demonstrates the synergy between remote sensing data and its versatile applications. Sentinel-1 offers invaluable open access to a wealth of radar imaging data. While these images serve a wide array of purposes, they are invaluable for climate-related research. Some applications are monitoring ice sheets and glaciers, mapping floods and wetland dynamics, detecting extreme weather events, and assessing soil moisture and vegetation dynamics, with the latter being particularly helpful for understanding agricultural water use. As a result, this open-access promotes a collaborative, data-driven approach towards a number of critical environmental issues.

Another beneficial feature of the Sentinel-1 mission is its relatively short revisit period. The mission consists of two satellites, Sentinel-1A and Sentinel-1B, with each being equipped with identical C-band SAR instruments. The two satellites, each having a revisit period of 12 days, traverse the same sun-synchronous orbit, 180^{O} apart. This configuration allowed the mission’s revisit time to be 6 days. Short revisit times are crucial because they allow for frequent monitoring of ‘fast’ processes like soil moisture variations, ultimately improving the accuracy of results (Wickel et al., 2001; Balenzano et al., 2011). In

this context, the Sentinel-1 mission's data, being open-source and suitable for agricultural applications, is the first source of radar data considered in this study.

However, Sentinel-1B experienced an anomaly on December, 2021, and was no longer operational; despite many efforts from the European Space Agency (ESA) and other concerned parties, the satellite issue could not be fixed (ESA, 2022). Since then, plans were made to launch Sentinel-1C as a replacement of the lost Sentinel-1B. This would be followed by a launch of Sentinel-1D, as a replacement for Sentinel-1A, which has already exceeded its expected lifetime. However, the initial launch attempt of Sentinel-1C, on board of the Vega-C rocket, was not successful due to the failure of one of the rocket's components (ESA, 2023). Since then, despite some initial promises of it being launched before the end of 2023, the next launch date still hasn't been set, with other sources claiming that the next launch is not expected any time before late 2025 (Foust, 2023). In the meantime, this loss means that the Sentinel-1 mission, now comprising of just one operational SAR, the Sentinel-1A, has a revisit period of 12 days. This significantly limits its effectiveness in future studies and applications, namely in this paper's topic of interest, which is irrigation quantification through soil moisture estimations.

This incident with Sentinel-1B only serves as a reminder of the importance of continuously searching for alternative data sources, so as to decrease over-reliance and to be better prepared to handle any issues that arise with a data source. It also highlights the importance of improving the existing methodologies by taking advantage of new data sources that are being made available. In this context, investigative efforts were made to find alternative SARs and missions whose data could potentially be used, either as a substitute or in integration, with the Sentinel-1 data. They are described in the next section.

As for this study, it relies on 265 separate Sentinel-1 images. The images obtained contain incidence-angle-dependent backscatter measurements, measured by the C-band sensors (CSAR) present on the two satellites. They were acquired using the Interferometric Wide-swath (IW) mode, which is the mission's main operational mode over land. This mode is commonly used in large-scale applications, as the extensive swath widths offered by these acquisitions is a very favorable attribute, which allows them to easily cover significant portions of agricultural areas. The data used is backscatter and incidence angle data from the Vertical-Vertical (VV) polarization of Ground-Range-Detected at High resolution (GRDH) products. Their pixel spacing is 10 m, yielding a 20 x 22 m nominal spatial resolution; their radiometric accuracy is 1 dB (3σ) (Torres et al., 2012).

The acquisition dates stretch between 2020-01-01 and 2022-12-28. For the first period (2020-2021), images were obtained both from Sentinel-1A and Sentinel-1B. In contrast, for the second period, (2022), due to the loss of Sentinel-B mentioned earlier, images were only acquired from Sentinel1-A. The area of interest is traversed by two different satellite orbits from Sentinel-1, whose relative orbit numbers are 66 and 88. Due to the fact that the area of interest happens to lie very close to the boundary between two acquisition zones, there are some days in which two images were available. This enabled few retrievals to be captured from two slightly different incidence angles.

All the images underwent several processing steps, including several corrections, noise removal, and upscaling as necessary. These are elaborated in the discussion concerned with the implementation of the RT1 algorithm (Section 3.1.2).

2.2. Radar Data 2: Alternatives to Sentinel-1

The overall strategy to identify alternative SAR's to be used for agricultural applications, namely the modelling of soil moisture dynamics, consists of multiple steps and is described as follows. The first step

is to come up with a preliminary list of possible alternatives to Sentinel-1 by searching the literature online. Then, this list is filtered based on criteria that align with the project's purpose and considering Sentinel-1 as a reference or baseline for all criteria assessments. The criteria can be split into two groups: technical requirements and data requirements.

Starting with the technical requirements, the first condition is for the candidate to be a SAR that is still operating/functional. This is necessary because an obsolete SAR cannot be helpful for any monitoring project in the future. Two other criteria are the spatial and temporal resolutions. They must be adequate to fulfill the intended use. Regarding the temporal resolution, there are two main points to note. The first point, already discussed in the previous section, is the small timescale at which soil moisture variations can occur (Haiyan & Hai-Mei, 2021). The second point is the lag between the beginning of water-stress felt by a plant, detecting the deficiency, and possibly taking the necessary corrective measures to limit the impacts of that stress. Therefore, a high temporal resolution is a crucial factor; consequently, it's required to be in the order of a few days. As for the spatial resolution, a relatively fine resolution is also important due to the inconsistent nature and accordingly the significant spatial variability of soil layers and their properties. Low resolutions would lead to oversimplified results that merge large, heterogenous areas into one cell and are thus not representative of reality. In this context, if the SAR mission is to be considered as an alternative source to Sentinel-1A, the spatial resolution should preferably be in the range of 10-100 m and the temporal resolution should preferably be higher than that of Sentinel-1A, so less than 12 days. A fourth technical criterion is the swath dimensions. The SAR image should be large enough to cover the agricultural field(s) considered. This particular study's area of interest is limited to approximately 73km^2 of agricultural areas, which fall roughly within a bounding box of 19 x 20 km. However, generally, larger swath widths are preferred since they allow future studies to be done at larger scales, which is one of the main advantages of remote sensing. Other technical specifications include the polarization, which could be single, dual, or quad-polarization, and the radar band, which is preferably C-band considering the trade-off between wavelength and penetration depth (Singh et al., 2018). However, the polarization modes offered and the radar bands used by a SAR are not considered as deciding factors in its inclusion or exclusion from the final list of potential alternatives. Nonetheless, they are factors to be accounted for when comparing the performance of the different SARs in monitoring the soil moisture dynamics. SARs that were not operational during the period of 2020-2021 are excluded as this period, during which both Sentinel-1A and Sentinel-1B were still operational, will be used as the baseline period for the comparison. The list of SARs fulfilling the above criteria, categorized as "technical requirements", is displayed in the table below.

Table 1 - List of alternative SARs that were investigated

Mission Name	Nation	Satellites	Space Agency	Radar Band	Revisit period [days]	Resolution [m]	Max Swath Width [km]	Polarization Modes	Lifetime
Sentinel-1	Europe	1 (Sentinel-1A)	European Space Agency (ESA)	C	12	5-20	400	Dual (VV/VH or HH/HV)	2014-P
Gao Fen - 3	China	1 (Gao Fen - 3)	China National Space Administration (CNSA)	C	3	1-500	650	Quad (HH/HV/VH/VV)	2016-P
Radarsat-2	Canada	1 (Radarsat-2)	Canadian Space Agency (CSA)	C	24	1-100	500	Quad (HH/HV/VH/VV)	2007-P
Capella	US	10	Capella Space Corporation	X	<1	0.5-11.5	10	Single (HH/VV)	2020-P

TerraSAR-X	Germany	1 (TerraSAR-X)	German Aerospace Center (DLR)	X	11	0.25-40	200	Dual (HH/HV or VV/VH)	2007-P
COSMO-SkyMed	Italy	4 (COSMO-SkyMed 1,2,3,4)	Italian Space Agency (ASI)	X	<1	1-100	200	Quad (HH/HV/VH/VV)	2007/2010-P
ALOS-2	Japan	1 (PALSAR-2)	Japan Aerospace Exploration Agency (JAXA)	L	14	3-100	490	Quad (HH/HV/VH/VV)	2014-P
SAOCOM	Argentina	2 (SAOCOM 1A, 1B)	Argentine Space Agency (CONAE)	L	8/16	10-100	350	Quad (HH/HV/VH/VV)	2018/2020-P
PAZ	Spain	1 (PAZ)	Hisdesat	X	11	0.25-40	200	Dual (HH/HV or VV/VH)	2018-P

To properly evaluate a SAR's suitability as an alternative, having sufficient technical requirements is not enough: it is essential to gather information about the availability of suitable images to be used as input for the analysis. This leads to discussing the data requirements, which include aspects such as if the data is open-access, browsable, purchasable (and some typical price ranges if so), and if there are alternative acquisition methods/opportunities, such as use cases for educational or research purposes. Regarding the choice of radar images, and elaborating on what is considered a "suitable" image, in order to ensure that the comparison is viable, the images to be chosen for the comparison should be taken around the same period or time of year (to limit effects of seasonality) and should have some spatial overlap (to have comparable climate/crop/soil). In this context, this step also includes browsing the archives for potential images that meet these criteria to get a more definitive idea about the feasibility and the potential scope of the comparative analysis that could be done.

So, for each of the SAR missions listed in Table 1, the main factors to consider can then be summarized into two criteria. The first criterion is accessibility, which can be split into the ability to browse the catalogue of available SAR products and the ability to obtain/acquire the images of interest. The second criterion is availability, which depends on whether the mission's catalogue actually contains any images that can be used in a comparative analysis. The results of this investigation into the considered SAR's (listed in Table 1) are summarized in the table below.

Table 2 - Results of investigation into alternative SAR's

Mission Name	**Data accessibility**		**Data availability**	**Main issue**
	Browsing	**Acquisition**		
Sentinel-1	Full access	Free	Good	--
Gao Fen - 3	Not browsable	300€ / image	--	Accessibility
Radarsat-2	Limited access: unprocessed images only	Application required	Fair	Revisit period
Capella	Limited access: sample only	Request required	Very limited	Data availability
TerraSAR-X	Full access	Application required	Limited	Spatial coverage, data availability, and accessibility
COSMO-SkyMed	Full access; form request required	--	--	Accessibility (Registration error)
ALOS-2	Full access; email request required	1500€ / image; broken link	Fair	Accessibility
SAOCOM	Full access; form & email requests required	--	--	Accessibility (Strict requirements)
PAZ	Full access; email request required	--	--	Accessibility (Broken link)

If suitable alternatives had been found, the next steps would have been to obtain the data necessary, in terms of radar images, proceed with the necessary pre-processing, attempt to use the processed images to obtain soil moisture estimations. Consequently, a comparative analysis would be done based on the results obtained from the different SARs considering factors such as precision, accuracy, as well as the differences in technical specifications and the procedure/methodology followed to obtain the desired output from the images.

Unfortunately, no proper alternative was found. As can be seen from Table 2, data accessibility is the main obstacle faced during the alternatives' evaluation. There's a significant difficulty in obtaining SAR mission data, whether due to high costs, broken links, errors in registration, or long request applications. Furthermore, in some cases, even browsing a mission's data is not possible, making it impossible to evaluate a-priori whether suitable images are available or not. In this regard, the study will rely only on Sentinel-1 data. This is discussed in further details in the methodology (Section 3).

2.3. Soil Moisture Data

This study follows the footsteps of Dari et al. (2023) in which high-resolution soil moisture data was obtained using the RT1 approach. In this context, the soil moisture data used in the SM-inversion algorithm is "computed", not "acquired". In fact, soil moisture is the main parameter of this study; it is the main output of the RT1 algorithm and, as the name suggests, the main input for the SM2Rain algorithm. The reasons behind this are explained in greater detail in the theoretical background section (Section 3.2.1). Details about the methodology, including both the theory it's based on and how it was specifically implemented in this study to obtain the soil moisture data, are discussed in Section 3.1.

The obtained soil moisture data consists of a timeseries, gridded at 500 m sampling based on the chosen target grid for the study. It represents a percentage; thus, its theoretical ranges are 0 to 1, with a physical unit of m^3 of water per m^3 of soil. It extends over the years of 2020-2022, and is split into two periods: the first period covering the years 2020-2021 and the second covering the year of 2022. The main reason behind this split is the stark difference in availability of radar data, due to the loss of Sentinel-1B at the end of 2021. Another reason is the use of the first period for model fitting and the second period for estimation and validation.

2.4. Potential Evapotranspiration Data

Potential evapotranspiration (PET) data is another important input for the soil water balance represented by the SM-based inversion algorithm. In this study, temperature and radiation data are used to obtain PET values, using the Hargreaves formula (Equation (24)). In this context, PET is also "computed". The reasoning behind this choice, in addition to the procedure followed to obtain the data, is explained in detail in Section 3.2.

The PET data used as input in the SM-based inversion algorithm is computed at the daily timescale and measured in mm/d, covering the period of 2020-2022.

2.5. Meteorological Data

Meteorological data needed for this study consist of two main parameters: temperature and rainfall/precipitation. Temperature data is used to calculate PET values. Rainfall data is used as input for

the SM-based inversion algorithm. Due to the fact that the fitting of most of the algorithm's parameters is dictated and largely influenced by rainfall (Section 3.2.2), this choice was made after very careful consideration. Considering the study's relatively limited spatial scale, using ARPA's gridded dataset, was deemed not appropriate. In contrast, the most appropriate choice, both in terms of reliability and representativeness, was to rely on locally measured data from the Caluso meteo-station, which lies at the heart of the study area.

In this context, both the temperature and precipitation datasets are obtained from ARPA Piemonte's website. The data collected is specifically that of the Caluso station, for the study period of 2020-2022. Both datasets consist of data at the daily timescale. The precipitation data is measured in mm/d. The temperature data, consisting of minimum, maximum, and average temperature per day, is measured in °C.

The location of the Caluso station is shown in the figure below.

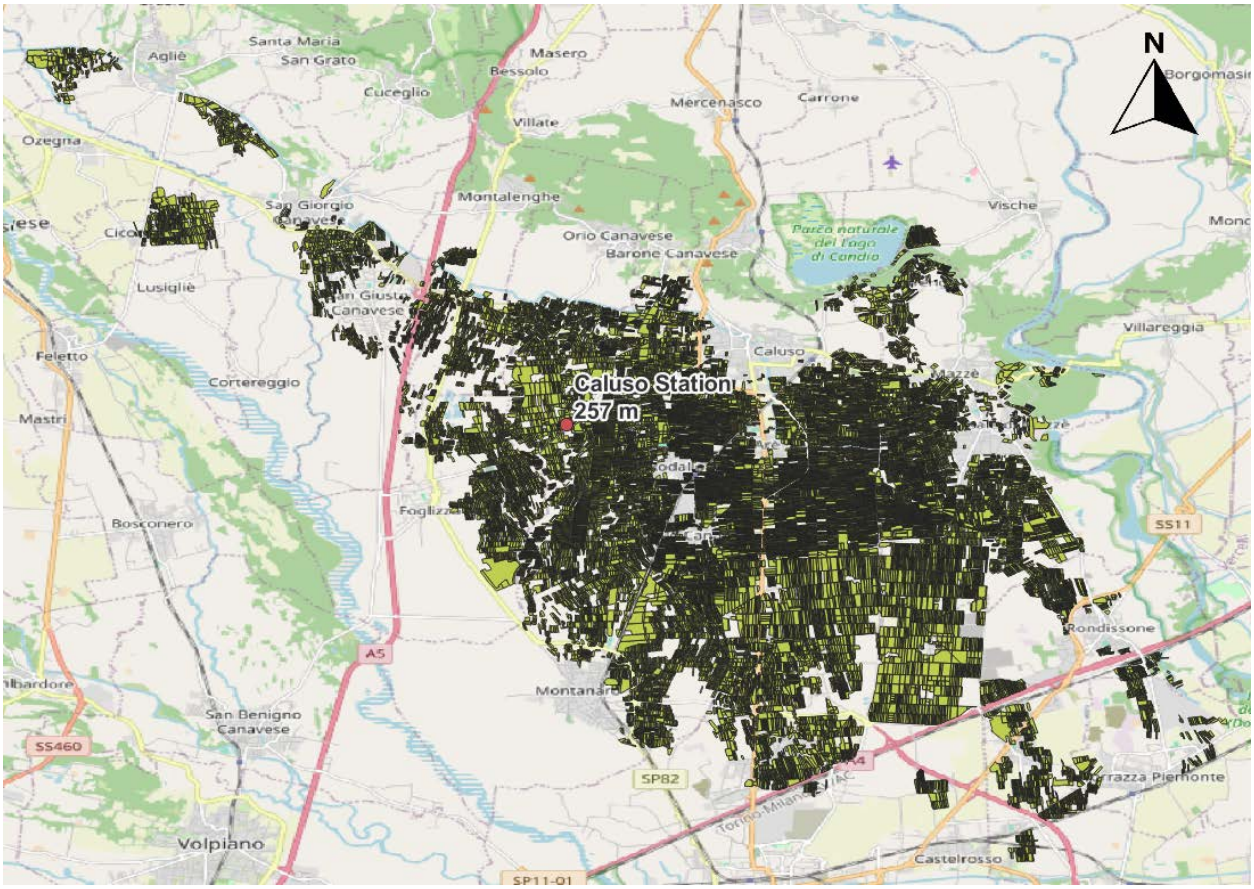

Figure 2 - Map showing location of chosen station for meteorological data (using QGIS and OpenStreetMap)

2.6. Reanalysis Data

Two datasets were obtained in the form of reanalysis data: the Leaf Area Index (LAI) and baseline soil moisture. They were specifically obtained from "ERA5-Land hourly data from 1950 to present" open database (Muñoz Sabater, 2019), which was downloaded from the Copernicus Climate Change Service (2024). The results contain modified Copernicus Climate Change Service information 2024. It must be

noted that neither the European Commission nor ECMWF is responsible for any use that may be made of the Copernicus information or data it contains.

The acquired data extended over the latitude ranges from 7.7 to 8^{O}E and longitude ranges from 45.1 to 45.4^{O}N to ensure coverage of the whole AOI. Moreover, their temporal range covered the complete time period of 2020 to 2022, covered in this study.

As described by Muñoz Sabater (2019), ERA5-Land is a reanalysis dataset generated "by replaying the land component of the European Centre for Medium-Range Weather Forecasts (ECMWF) ERA5 climate reanalysis". Reanalysis typically relies on physical laws to integrate measured or observed data (from many sources over the world) with modelled data in an attempt to yield datasets that are considered globally complete and consistent.
The two parameters obtained from the ERA5-Land dataset are listed in the table below.

Table 3 - Reanalysis parameters obtained from C3S (2024)

Abbreviation	ID	Name	Unit	Description (Muñoz Sabater, 2019)
lai_lv	66	Leaf area index, low vegetation	m^2 leaves / m^2 land	''This parameter is the surface area of one side of all the leaves found over an area of land for vegetation classified as 'low' (e.g. crops and mixed farming, irrigated crops, short grass, tall grass, tundra, semidesert, bogs and marshes, evergreen shrubs, deciduous shrubs, and water and land mixtures)''.
swvl1	39	Volumetric soil water layer 1	m^3 water / m^3 soil	"This parameter is the volume of water in soil layer 1 (0–7 cm, the surface is at 0 cm)".

lai_lv data was used within the RT1 algorithm to account for some of the temporal variability of the vegetation optical depth, specifically for its seasonal variations.
The swvl1 data was considered as the reference or baseline soil moisture data for the evaluation of the fitting results obtained from the RT1 algorithm. It was also used as a benchmark to scale the algorithm's N parameter, one of the main outputs obtained from the fitting, to actual SM timeseries. These uses are explained in detail in the section describing the implementation of the RT1 approach in this study (Section 3.1.2).

2.7. Benchmark Irrigation Data

Due to lack of irrigation volume data for Canale Caluso, reference irrigation data is limited to irrigation calendars, presented in the figure below.

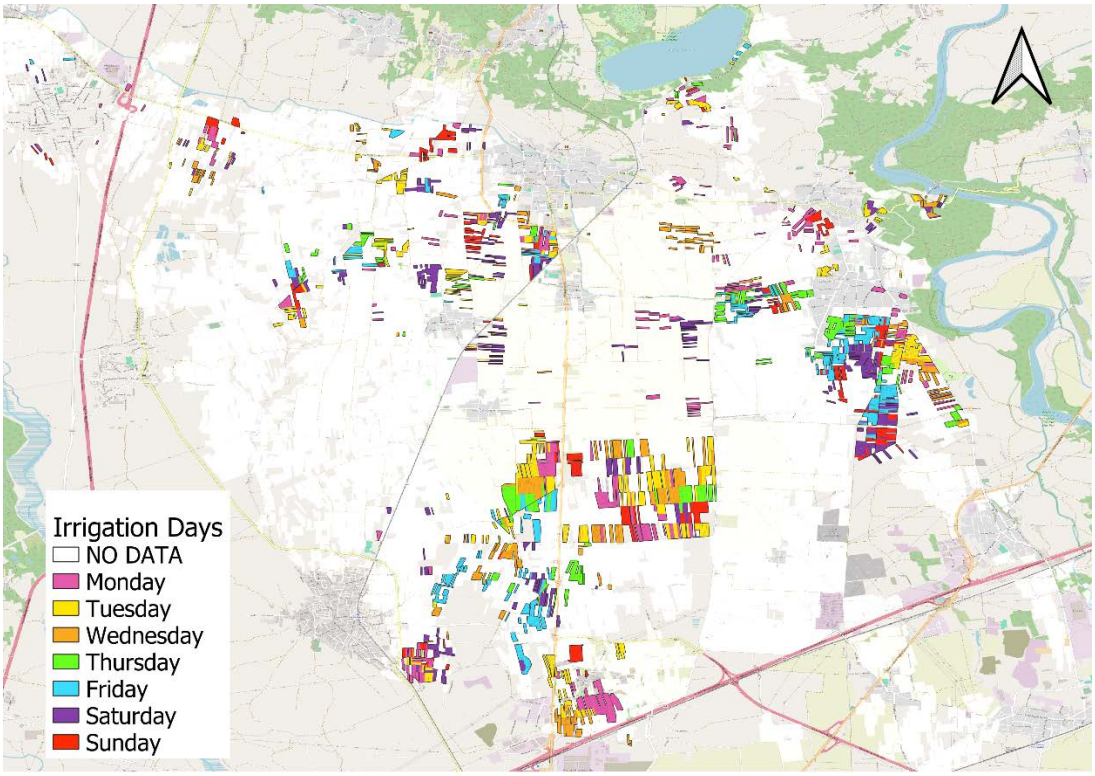

Figure 3 – Map showing irrigation calendar data obtained from Consortium of Caluso Canal (using QGIS and OpenStreetMap)

As can be seen in Figure 3, the irrigation calendar covers a subsection of the considered agricultural areas, where the areas with irrigation data are colored and the ones without this data are displayed in white. In fact, the total area covered by the irrigation calendar data is 7.48 km^2, which accounts for approximately 10 % of the total agricultural areas of interest (Table 4). The data is given in the form of the day of week on which a certain agricultural field is irrigated. The irrigation is done between the months of May and September, with the most significant volumes being utilized between the months of June and August.

Table 4 - Statistics for irrigation calendar data

Irrigation Day	Area [km^2]	Percentage of Total Area [%]	Percentage of Areas with Irrigation Data [%]
Monday	1.24	1.71	16.54
Tuesday	1.29	1.78	17.28
Wednesday	1.15	1.59	15.40
Thursday	0.87	1.20	11.60
Friday	0.99	1.36	13.20
Saturday	1.11	1.52	14.77
Sunday	0.84	1.15	11.20
Areas with Irrigation Data	**7.48**	**10.31**	**100.00**
Areas without Irrigation Data	**65.10**	**89.69**	**-**
Total Area	**72.58**	**100.00**	**-**

This data was obtained directly from “Il Consorzio del Canale Demaniale di Caluso” (The Consortium of the Caluso State Canal), which is the authority responsible for the management of the Caluso Canal. It was used in the analysis of soil moisture data obtained from the RT1 algorithm (Section 4.1.3).

3. METHODOLOGY

As already mentioned, the basis for the adopted methodology are the studies of Quast et al. (2023), to obtain SM estimates from Sentinel-1 data via the RT1 approach, and Dari et al. (2023), to obtain irrigation estimates from SM data via the SM-based inversion approach.

The aim of the first paper, by Quast et al. (2023), was, in fact, to confirm the feasibility of using Sentinel-1 data as input for RT1, which originally relied on scatterometer data. It thoroughly analyzes this shift in the nature of the input radar data, discusses its impacts and limitations, and suggests very useful modifications to deal with them.

The latter paper, which was part of the European Space Agency's (ESA) Irrigation+ project, produced the first high-resolution (~1 km), regional-scale irrigation water data sets via a slightly modified version of the SM-based inversion approach. Its authors were able to do so by relying on high-resolution SM data, as opposed to the approach's original study (Brocca et al., 2018), which relied on coarse-resolution SM data instead. In fact, in order to obtain the high-resolution SM data, the authors of Dari et al. 2023 adopted the RT1 approach mentioned previously for two of the three basins considered in that study (Ebro and Po).

Consequently, the methodology for the RT1 and that for the SM-based inversion approach, also referred to as SM2RAIN, are both discussed below.

3.1. First-order Radiative Transfer (RT1) Model

3.1.1. Theoretical Background

The radiative transfer equation (RTE), initially published by Chandrasekhar (1960), considers three main characteristics to describe the scattering behavior within a scattering and absorbing volume: an extinction coefficient, a scattering coefficient, and a scattering phase function, with the first two governing the amplitude of some radiation behavior, and the third mainly representing the direction component. As for the behavior after hitting the boundary of a rough surface, it can be described by what is called a Bidirectional Reflectance Distribution Function (BRDF) and a roughness coefficient.

Considering the case of radiation reaching a SAR after hitting the surface of an agricultural area, this radiation can be split into several categories, based on the elements it interacted with throughout its path. The different waves could have interacted with soil, vegetation, or a combination of the two. Waves that interact with both surfaces, passing only once onto each surface, can be considered as first-order interactions. Consequently, those that undergo a sort of back-and-forth, thus interacting with one of the two surfaces more than once before eventually heading back to the SAR, would consist of higher-order interactions. They are also referred to as the "bistatic" component of radiation scattering, as opposed to the waves that interact with just one element, which represent the "monostatic" component of scattered radiation (Quast et al., 2023). The scheme, displayed in the figure below helps visualize the different paths discussed above.

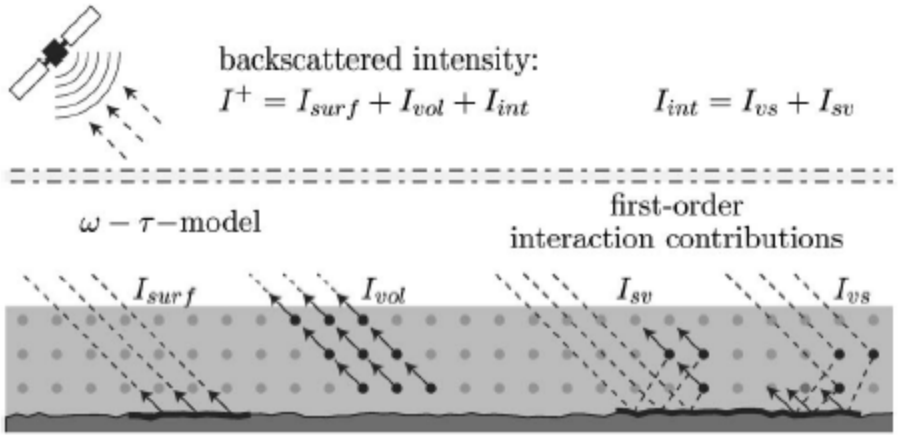

Figure 4 - Scheme displaying the different contributions to backscatter radiation received by a SAR (Quast et al., 2016)

Given this context, it is explained in the study of Quast et al. (2016), how, due to the complex nature of scattering behavior induced by vegetation, most of the early studies adopted "a zero-order approximation of the solution to the RTE". In other words, only the radiation that's directly reflected back after hitting one surface was properly considered; that is, any interactions of the first-order or higher orders were poorly accounted for. This was mainly due to two requirements needed to consider higher order interactions. The first requirement is the intensive computational power and the second is knowing the bistatic scattering properties of the soil and the vegetation cover being considered. This led to the adoption of analytical functions in order to better approximate first order interactions while limiting the computational power needed to do so.

This is explained extensively in a following study, done in 2019, which comprises a thorough application of the suggested method. As explained in Quast et al. (2019), the first-order radiative transfer model (RT1) is a generic, semi-empirical model that uses scatterometer measurements to obtain soil- and vegetation-related parameters. The parametrization framework for the model can be considered as a generalization of the water-cloud model (Attema & Ulaby, 1978); it considers that a canopy, being a mix that is predominantly made of air (space between the leaves) and water (moisture contained in the vegetation), can be modeled as a water-cloud.

It relies on a BRDF to describe the scattering behavior of bare soil. As for vegetation, it relies on a scattering phase function, $\hat{p}$. However, instead of describing extinction and absorption coefficients, it introduces two parameters: the optical depth, τ [-], and the single-scattering albedo, ω [-]. This leads to the equation below.

$$\sigma_0 = 4\pi \cos(\theta_0) \left[f_{bs} \underbrace{\cos(\theta_0)\, BRDF}_{bare\ soil\ contribution\ (\sigma_0^S)} + (1 - f_{bs}) \left(\underbrace{\gamma^2 \cos(\theta_0)\, BRDF}_{vegetation-covered\ soil\ contribution\ (\gamma^2 \sigma_0^S)} + \underbrace{\frac{\omega}{2}(1 - \gamma^2)\, \hat{p}}_{vegetation\ contribution\ (\sigma_0^v)} + \underbrace{\sigma_0^{int}}_{interaction\ contribution} \right) \right] \quad (1)$$

where θ_0 [rad] is the viewing zenith angle, f_{bs} [-] is the fraction of bare-soil covering the area of interest, and γ [-] is the 2-way attenuation factor, defined as:

$$\gamma^2 = e^{-\frac{2\tau}{\cos(\theta_0)}} \tag{2}$$

A visual representation clarifying what each term represents is shown in the figure below.

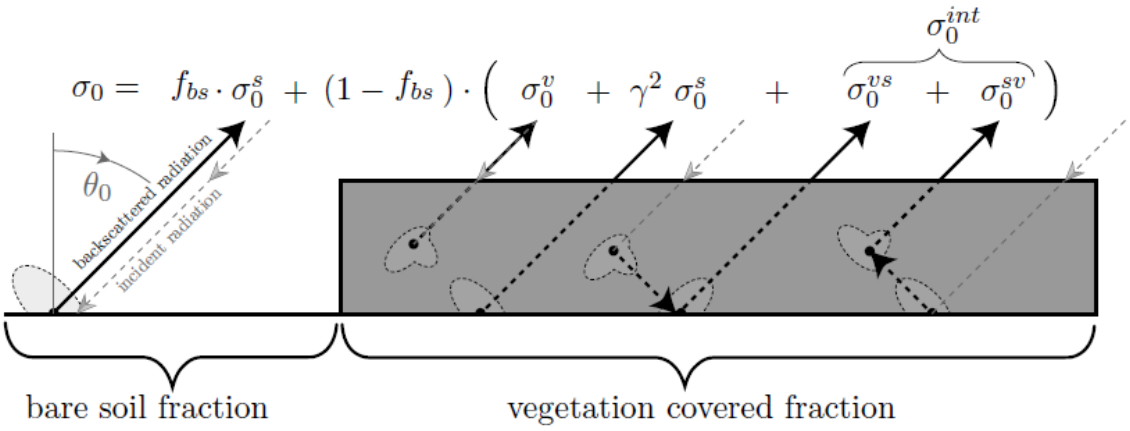

Figure 5 - Alternative scheme showing individual contributions to backscatter signal (Quast et al., 2019)

Having set the general foundations on which this approach is based, the following studies of Quast et al. (2019, 2023) tackle a large number of issues regarding the practical implementation of this approach. They are discussed separately in the subsections below.

Choice of a Surface BRDF

The possible choices for a bare soil scattering model that exist in literature are numerous. However, as previously discussed in Section 3.1.1, most of the semi-empirical models available neglect the first-order contributions (Quast et al., 2023). In contrast, there are more robust models, namely the Integral Equation Model (IEM) (Álvarez-Pérez, 2001) or its derivatives, the IEM2M (Álvarez-Pérez, 2012), and AIEM (Chen et al., 2015) that would allow a thorough description of this scattering. However, their use within the suggested non-linear fitting procedure requires large computational power and, consequently, isn't yet scalable. This led to the adoption of the generalized Henyey-Greenstein (HG) phase function, described in the equation below (Quast et al., 2019, 2023).

$$BRDF(N, t, a) = \frac{N}{R_0(t, a)} HG\left(t, \tilde{\Theta}_a\right) \tag{3}$$

where:

$$HG(t, \Theta) = \frac{1}{4\pi} \frac{1 - t^2}{[1 + t^2 - 2t\cos(\Theta)]^{\frac{3}{2}}}$$

$$\tilde{\Theta}_a = a\cos(\theta_0)\cos(\theta_S) - \sin(\theta_0)\sin(\theta_S)\cos(\phi_0 - \phi_S)$$

$$R_0(t, a) = \frac{1 - t^2}{2a^2t^2}\left[\frac{(1 + t^2 + at) - \sqrt{(1 + t^2 + 2at)(1 + t^2)}}{\sqrt{(1 + t^2 + 2at)}}\right]$$

The angle pairs (θ_0, Φ_0) [rad] and (θ_S, Φ_S) [rad] represent the direction of the incident and scattered radiation respectively, N [-] represents the nadir ($\theta_0 = 0$) hemispherical reflectance. t [-] represents a directionality parameter (where a Lambertian surface would have t=0 and a mirror would have t=1), and a [-] represents an anisotropy parameter (where a<0 would mean that backward-scattering is favored and a>0 would mean that forward-scattering is more dominant). The main parameter of interest from the above equation is the parameter N, which primarily influences the magnitude of the BRDF. As a result, it can be directly "related to the soil-permittivity ϵ and consequently, in the microwave-domain, to soil moisture" (Quast et al., 2023).

Choice of Vegetation Scattering Phase Function, $\hat{p}$

As already mentioned, the scattering behavior of vegetation is described via two main parameters, the optical depth, τ, and the single-scattering albedo, ω, in addition to a phase function $\hat{p}$. In Quast et al. (2019), the phase function considered was a linear combination of three HG functions. This was possible because that study relied on ASCAT scatterometer data, which has multiple acquisitions from different incidence angles, and which, in turn, made it possible to have an unambiguous retrieval of ω and $\hat{p}$. In Quast et al. (2023), however, which relies on Sentinel-1 data that is typically limited to only one incidence angle per acquisition, this unambiguous retrieval was not possible. As a result, the chosen phase function was "Isotropic", which is basically a HG function with t set to 0, described by the equation below.

$$\hat{p}(\Theta) = \frac{1}{4\pi} \tag{4}$$

Definition of Cost Function and Method for Fitting Procedure

The fitting procedure is done cell-by-cell. The adopted cost function is RMSE where the error is the difference, for each observation, between the modelled and observed backscattering, as shown in the equation below (Quast et al., 2019, 2023).

$$RMSE = \sqrt{\sum(\sigma^0_{observed} - \sigma^0_{modeled})^2} \tag{5}$$

The observed backscatter is the one obtained from the Sentinel-1 data while the modeled backscatter is calculated using Equation (1). In both Quast et al. (2019) and Quast et al. (2023), the fitting was done based on a "Trust Region Reflective" non-linear least-squares fitting.

Connection to Biophysical Variables

Two of the procedure's parameters, τ and N, can be linked to biophysical variables.

The optical depth, τ, represents some of the temporal variability, more specifically, the seasonal dynamics, of vegetation. N, on the other hand, as already mentioned after its introduction in Equation (3), is strongly linked to soil moisture.

In this context, in the study of Quast et al. (2019), these model parameters were linked to biophysical variables, by assuming a linear relationship between them, through simple empirical relations shown below.

$$\tau = v_2 \times LAI \quad (6)$$

$$N = s_2 \times SM \quad (7)$$

In that study, different test types, including forward simulations and backward inversions, were done over specific test sites for which auxiliary data for LAI and SM were available. This auxiliary data, consequently, served as a reference based on which several numerical values, such as those of s_2 and v_2, were then set and adjusted. In other words, the values of s_2 and v_2 were chosen and tuned such that the obtained LAI and SM values are comparable to those of the reference datasets.

Choice of Parameter Specifications

Constraints were set for each of the model parameters, mainly regarding their temporal and spatial variability. In summary, it was found most suitable to represent the temporal variability through two parameters: the optical depth, τ, and the BRDF's nadir hemispherical reflectance, N.

Spatial variability, on the other hand, was limited to four parameters: the bare-soil fraction, f_{bs}, the single-scattering albedo, ω, the coefficient of asymmetry, t, and the coefficient of proportionality linking N to SM, "s_2".

The three parameters to be fitted are N, ω, and t. As already mentioned, all three parameters vary spatially, which is why the fitting procedure is done cell-by-cell. t is also referred to as t_S, since it's the t parameter within the BRDF, that is, within the soil's scattering function.

Since N is linked to SM, which is expected to vary temporally, N is also given the freedom to vary temporally and is, hence, optimized for each observation. Furthermore, it is proposed in the study of Quast et al. (2019) that, considering Kirchhoff's law of thermal radiation and C-band emissivity values that were measured empirically, it is not physically plausible for N to exceed 0.1.

ω, on the other hand, which represents a value for albedo, is expected to vary as a function of the angle from which an acquisition is done. As a result, it is optimized for each Sentinel-1 orbit. Furthermore, given that this procedure deals with agricultural areas comprising of a mix of soil and vegetation which naturally don't have extremely high albedo values, an upper limit of 0.5 is set for this parameter.

Considering that t_S describes the directionality of soil scattering, which is considered a characteristic of the soil itself, it is assumed that this parameter does not have any temporal variability. Consequently, one value of t_S is optimized for each considered cell in the fitting. An upper limit of 0.5 is again considered. It should be noted, however, that this parameter largely dictates the contribution of the bistatic scattering. To obtain proper estimates for this bistatic component of scattering, it is necessary to have bistatic measurements (i.e., measurements taken from multiple angles) as input. Therefore, in the case of Sentinel-1 images, which consist of monostatic measurements (i.e. measurements with a very limited range of incidence angles), the obtained estimations for the first-order interactions can only be considered as "best-guesses" (Quast et al., 2023).

Regarding s_2, given that's it's a completely empirical parameter, its range is restricted with the sole purpose of guaranteeing that N remains below its set upper limit of 0.1 (Quast et al., 2019).

3.1.2. Implementation of RT1 Algorithm

While the studies of Quast et al. of 2016 and 2019 laid the important foundations of the theory and implementation procedure for the RT1 procedure, one of the main takeaways was that, despite the approach's flexibility, a lot of the choices, such as the choice of parametrization functions and the constraints given to the different variables in terms of temporal and spatial variability, should be done based on the specific backscatter dataset being used. The characteristics of the available dataset, thus, largely affect which simplifications are needed or deemed suitable in order to obtain unambiguous fitting results. In this context, the specific implementation done in this study will mainly rely on the more recent study of Quast et al. (2023). The purpose of that study was specifically to analyze the feasibility of using Sentinel-1 data as input for the RT1 algorithm. Its study area was the catchment of the river Po. Thus, the agreement with that study in terms of both the source of backscatter data adopted and the study areas considered make it an optimal reference for the modelling and fitting choices to take within the implementation of the RT1 procedure, the bulk of which is elaborated in Section 3.1.2.4.

The whole RT1 procedure was done using the Python language, through original code, consisting of multiple scripts and functions, developed specifically for the purpose of this study. The processing, presentation, and analysis of this algorithm's results were done with the help of numerous open-source packages, most importantly: RT1 (Quast, 2023), xarray (Hoyer et al., 2024), rioxarray (Alan et al., 2024), pyproj (Alan et al., 2023), dask (Rocklin, 2015), numpy (Harris et al., 2020), scipy (Virtanen et al., 2020), pandas (The pandas development team, 2024), matplotlib (Caswell et al., 2024), and geopandas (Bossche et al., 2024).

3.1.2.1. Creation of a Target Grid:

As already discussed in Section 3.1.1, the two main inputs of the RT1 algorithm are Sentinel-1 data from different orbits and acquisitions and having a nominal resolution of 20 x 22 m, in additional to LAI data, obtained from a reanalysis dataset and having a nominal resolution of 9 km. Moreover, given that the target output resolution of the study is 1 km, this justifies the need to set a fixed target grid on which all other data can be stacked as deemed necessary. As a result, the first step of this study was to create this target grid. Its boundaries were set such that it encompasses the whole study area, with some adjustments to its exact borders to ensure a 500 m cell spacing, which would yield the 1 km resolution. This led to the creation of a 40 x 39 grid. The result can be seen in the figure below.

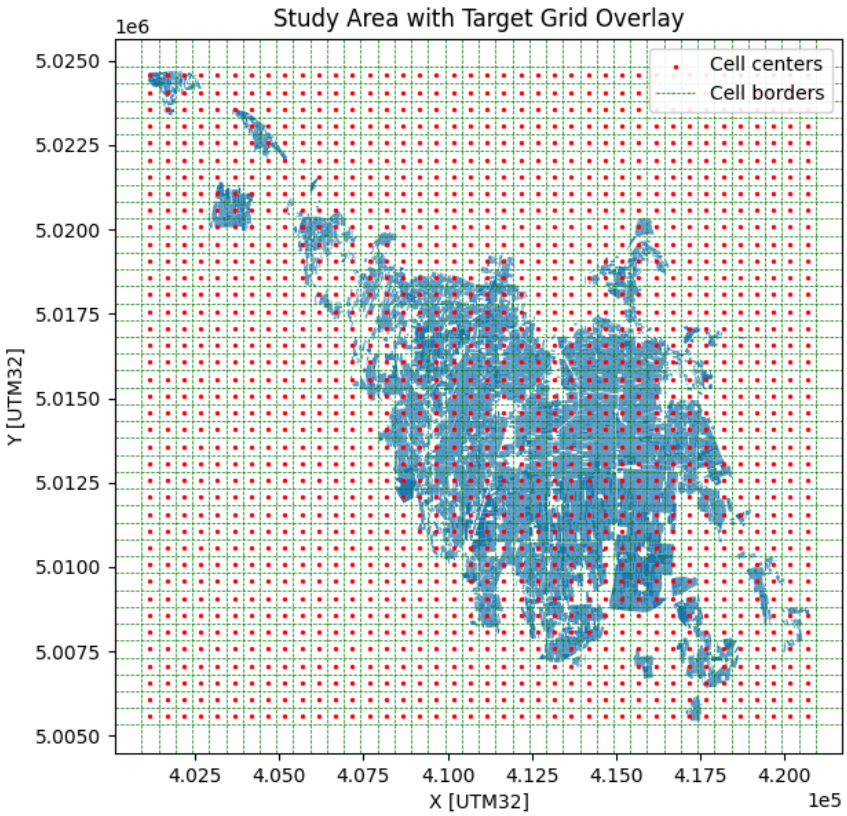

Figure 6 - Generated target grid, with 1 km spatial resolution, for the considered study area

Having set an appropriate target grid, the next steps are to process the two main datasets (Sentinel-1 and LAI) as needed to fill the grid with the inputs required for the RT1 fitting procedure.

3.1.2.2. Preparation of Sentinel-1 Data

Preprocessing

The first step in the preparation of the Sentinel-1 data described in Section 2.1 is preprocessing. It consists of five main steps: orbit correction, image border noise removal, radiometric calibration, speckle filtering, and terrain correction. These steps comply with those done by Quast et al. (2023) and with the "standard" preprocessing procedure described by Filipponi (2019). The output of this step is calibrated Sentinel-1 images having one backscatter and incidence angle value for each 10 m cell in the grid.

Downscaling

The second preparation step is downscaling these images to 500 m cells, so to the spatial resolution of 1 km and loading them into the target grid. The need for this downscaling is very well explained in the paper of Bauer-Marschallinger et al. (2019), which also proposes a robust methodology for doing it. They explain that the RT1 procedure relies on coarse-scale data to relate backscatter signals to soil and vegetation dynamics. Consequently, very small-scale data would capture individual ground features, leading to unwanted noise, which, in turn, would yield unsatisfactory SM estimates.

The processed sentinel data, hence, follow a slightly modified procedure to the one suggested by Bauer-Marschallinger et al. (2019), for the downscaling, which is explained as follows.

The procedure basically consists of several "masking" steps, where some cells are discarded based on specific criteria. This is followed by the aggregation of backscatter and incidence angle values via the arithmetic mean of values from whatever cells remain unmasked, and the assignment of the computed means to the corresponding cells in the target grid.

The first masking step, referred to as dynamic filtering, involves discarding cells with extremely high (> -5 dB) and extremely low (< -20 dB) backscatter values, since they're not expected to carry information about soil moisture (Bauer-Marschallinger, 2019). All cells whose backscatter values fall within these two thresholds will be hereby referred to as "valid" cells. Next, all cells that fall outside the agricultural areas, shown in Figure 1, are also discarded. All cells who fall within the agricultural areas will be hereby referred to as "agricultural" cells.

To help clarify the remaining steps, one additional terminology is defined. Considering a specific 500 m cell, with coordinates (X_t,Y_t), in the target grid, then all the 10 m cells with coordinates (X_i,Y_i) where $X_t - 250 < X_i < X_t + 250$ and $Y_t - 250 < Y_i < Y_t + 250$, that is, all the 10 m cells that would be contained within its borders, represented by green dashed lines in Figure 6, are hereby referred to as "proximate cells".

Then, according to Quast et al. (2023), backscatter and incidence angle data is aggregated from the 10 m cells and assigned to the 500 m target grid cells in all cases where more than 1 % of a target grid cell's proximate cells are "agricultural and valid". As mentioned previously, this aggregation is done via the arithmetic mean. That is, for each 500 m cell in the target grid, the backscatter value assigned to it is the arithmetic mean of the backscatter values from all valid, agricultural, proximate 10 m cells. Similarly, the incidence angle value assigned to it is computed as the arithmetic mean of incidence angle values for all valid, agricultural, proximate cells.

However, since the data assigned to a grid cell is supposed to represent a 500 x 500 m area, one additional condition is considered to ensure a minimal level of representativeness. The condition is that the total number of proximate cells is greater than 250. Given that the procedure aims to shift from a 10 m cell size to a 500 m cell size, then, theoretically, one cell in the target grid can contain up to 50 x 50 = 2500 cells from the original grid of the Sentinel-1 image. However, the Sentinel-1 dataset consists of images from different orbits and acquisitions, with different boundaries. Consequently, these images do not always overlap with the entirety of the study area. This implies the possibility that an image might cut-off somewhere in the middle of the study area, and thus the possibility that it might cut-off somewhere in the middle of the considered target grid, as demonstrated in the figure below.

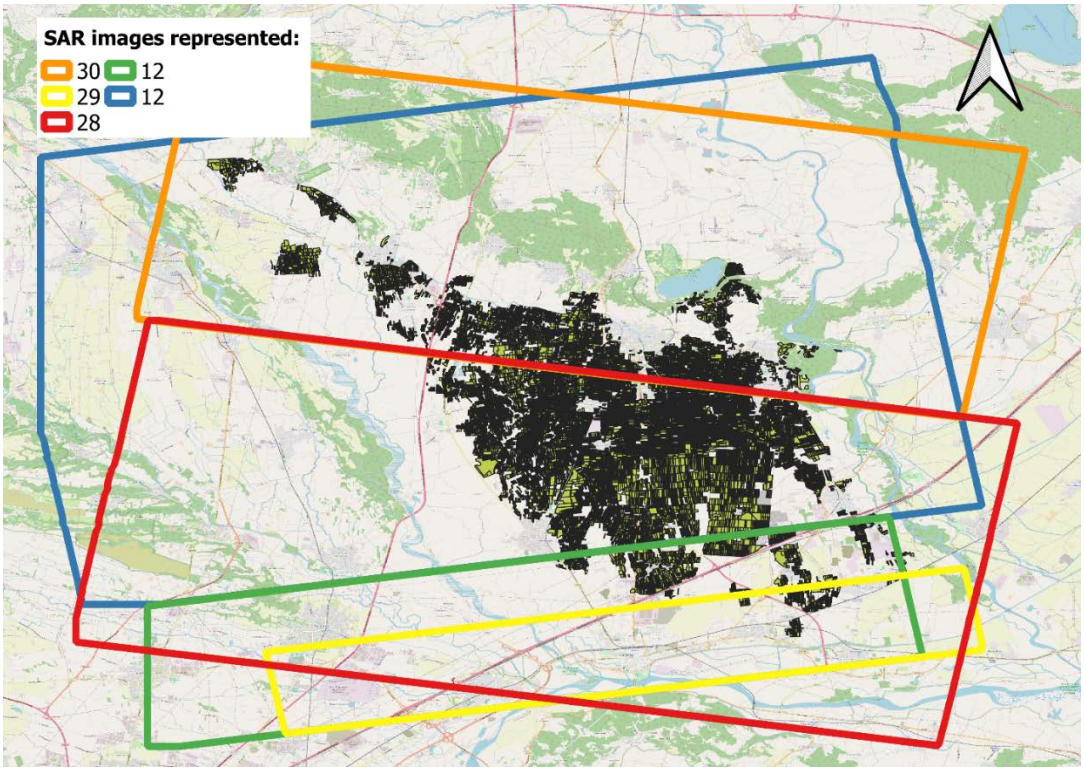

Figure 7 - Map displaying boundaries of sample SAR images that only partially overlap AOI (using QGIS and OpenStreetMap)

This condition, thus, ensures sufficient coverage by the Sentinel-1 image; more specifically, it ensures that the Sentinel-1 image covers at least 10% of a target cell's 500 m x 500 m area. It, therefore, avoids the possibility of representing a large target grid cell with data that originally covered, for instance, just 20 m x 20 m.

The final result obtained from this step is downscaled Sentinel-1 data. More specifically, the output is saved in tabular format, where each row contains the acquisition date, the grid cell coordinates, the relative orbit number of that acquisition, a backscatter value, and an incidence angle value. The acquisition date and relative orbit number were extracted from the metadata of the original Sentinel-1 images. The motive for extracting the relative orbit number is explained in the "Choice of Parameter Specifications" paragraph of Section 3.1.2.4.

3.1.2.3. Preparation of Reanalysis Data

As mentioned in Section 2.6, reanalysis data, more specifically LAI and swvl1 data, is initially obtained as hourly values with a resolution of 9 km or 0.1^{O}. Preparation of this data thus consists of modifying the temporal and spatial scales to fit those of the RT1's input (and output). The first preparation step is resampling or aggregating the hourly data into daily data. The second major step is assigning the resampled values to the corresponding cells in the target grid.

Resampling

The hourly data was aggregated into daily data by computing that arithmetic mean of the 24 hourly values for each day. The output from this step was hourly data for both LAI and swvl1.

Rescaling

Since the swvl1 data is meant to be used as baseline soil moisture data for the evaluation of the fitting procedure's output, no further processing was necessary. As for the LAI data, which is meant to be used as a proxy for the optical depth, τ, in order to account for some of the temporal dynamics of vegetation, one more step was required. The LAI data was scaled to the range of [0,0.5] and used as a direct substitute/equivalent to the τ parameter. This simplification was necessary due to the inability to provide an unambiguous parametrization of τ, and to avoid any jumps or data gaps that would worsen the SM retrieval (Quast et al., 2023; Dari et al., 2023). As for the choice of 0.5 as a maximum, this was based on the assumption that "at a spatial resolution of ~1 km we always expect a fraction of the pixel to exhibit no or only moderate vegetation cover" (Quast et al., 2023).

Value Assignment

Both the resampled swvl1 data and the resampled and rescaled LAI data have a lower resolution than that of the target grid. As a result, for each cell in the target grid, the corresponding reanalysis data was assigned based on minimum distance; that is, each grid cell was assigned the LAI and swvl1 values from the closest cell in the reanalysis grid for each acquisition date. The output after this step was then the addition of two columns: "tau", to represent the corresponding rescaled LAI values, and "swvl1" to all data rows obtained from the Sentinel-1 data preparation.

3.1.2.4. Retrieval Procedure / Parameter Fitting

The retrieval procedure consists of defining the functions to model soil and vegetation scattering behavior, setting constraints for all the algorithm's relevant parameters, defining the specific approach to do the parameter fitting, evaluating the fitting results, and finally the derivation of SM estimates. As already mentioned in Section 3.1.2, the retrieval procedure in this study will be largely based on the approach of Quast et al. (2023), which relies on the backscatter data from the same mission (Sentinel-1) and covers this study's AOI as well. The individual steps are discussed separately in the subsections below.

Choice of a Surface BRDF

The surface BRDF can theoretically be modeled via several phase functions such as Isotropic, Cosine Lobe, or Henyey-Greenstein. Alternatively, it could be modeled via a linear combination of multiple phase functions. The generalized Henyey-Greenstein phase function, defined in Equation (3), was chosen to represent the BRDF, as was done in Quast et al. (2023), and for the reasons mentioned in Section 3.1.1.

Choice of Vegetation Scattering Phase Function, $\hat{p}$

$\hat{p}$ can theoretically be modeled via phase functions such as Isotropic, Rayleigh, Henyey-Greenstein, or a linear combination of multiple phase functions. However, to avoid the issue of having an "under-determined" retrieval procedure, which is present in the case of using Sentinel-1 data, the Isotropic phase function, defined by Equation (4), was chosen as the vegetation scattering phase function.

Definition of Cost Function and Method for Fitting Procedure

As suggested by Quast et al. (2023), the chosen cost function is the RMSE, which is defined in Equation (5), and the fitting procedure is done based on the "Trust Region Reflective" non-linear optimization.

Choice of Parameter Specifications

The specifications chosen for the three parameters to be fitted are summarized in the table below.

Table 5 - Summary of the model parameters' specifications

Parameter	Lower Bound	Upper Bound	Starting Value	Frequency
N	0.01	0.075	0.025	Per observation
ω	0.01	0.5	0.25	Per orbit
t_S	0.01	0.5	0.2	Constant

The lower bounds, upper bounds, and optimization frequency for all three parameters, in addition to the starting values for N and t_S, were chosen in accordance with Quast et al. (2023). The reasoning behind the choice of lower and upper limits and the choice of optimization frequency is discussed in Section 3.1.1.

The choice of starting values for N and t_S is expected to be minimal. In contrast, given the limitations for the retrieval of the parameter ω (also discussed in Section 3.1.1) and the influence it has on the estimated backscatter component from vegetation, the starting value chosen for it can potentially have a significant impact on fitting results (Quast et al., 2023). In that study, three starting values, 0.05, 0.25, and 0.4, were tested to understand this impact. The results of that analysis showed that the starting value did have an impact in the case of densely-vegetated areas such as forests. Nonetheless, this impact was found to be minimal in the case of croplands, where results were highly consistent, regardless of the chosen starting value for ω. As a result, since the study area consists of croplands, the starting value chosen for ω, in this case, is not expected to have any impact on fitting results. Consequently, the middle value for ω, 0.25, which also happens to be at the center between the lower and upper bounds was chosen as a starting value in this study.

Execution of Fitting Procedure

The fitting of N, ω, and t_S was performed cell-by-cell, considering all the relevant cells in the target grid, using the latest available version (v2.0) of the open-source RT1 package (Quast, 2023). The RT1 package is a very powerful library that allows the definition of the different aspects of the fitting model, executes the fitting through efficient code, and facilitates the generation of informative plots to visualize the results.

In this context, the previously-prepared tabular dataset, obtained from the preparation of Sentinel-1 and reanalysis data, along with all the modelling decisions discussed above, such as the chosen scattering phase functions and the parameter specifications, were used as input for the RT1 module.

The output obtained from the module was fitting results for the three parameters N, ω, and t_S. These results were, then, combined with the input data, in the form of additional columns, "N", "omega" and "ts".

3.1.2.5. Evaluation of Fitting Results

The evaluation of fitting results was centered around checking the correlation between the main target parameter, N, which is assumed to be linearly related to SM, and baseline SM data (Quast et al., 2023).

The baseline SM data considered is the "swvl1" data, which was obtained from the ERA5-Land reanalysis dataset (Muñoz Sabater, 2019) (Section 2.6), and then resampled to the daily timescale (Section 3.1.2.3) for this purpose.

The metric used for the evaluation of fitting results is the Pearson correlation coefficient.

3.1.2.6. Derivation of Soil Moisture Estimates

As already discussed in Section 3.1.1, and as indicated in Equation (7), SM estimates are derived from N by scaling the obtained N values via the empirical parameter s_2, with the values of s_2 being picked such that N and SM values remain within reasonable ranges. In fact, in the study of Quast et al. (2019), they based their choice for values for s_2 on two considerations: the upper limit of their reference SM dataset and the upper limit of N. In their study, with N being bounded at 0.1 and SM being bounded at 0.45, their resulting range for s_2 was [0.1, 0.3].

Given the largely empirical nature of the scaling adopted by previous studies, four methods to scale from N to SM were tested in this study.

The first approach consists of scaling from N to SM via s_2, which, in turn, is computed based on the maxima of N and SM, in accordance with Quast et al. (2019). More specifically, one s_2 value was obtained for each cell, as the ratio between the maximum N value and the maximum swvl1 value. Then, SM values were obtained by dividing each observation's N value by the computed s_2 value for that cell.

The second and third approaches, in turn, are very similar to the first approach, as they also compute an s_2 value, with the only difference being which statistical parameter was considered to compute s_2.

Instead of relying on the maxima, the second method was a "minima-driven" scaling, as it computes s_2 as the ratio between the minimum N value and the minimum swvl1 value for each cell.

The third method is a "mean-driven" scaling, as it computes s_2 as the ratio between the mean N value and the mean swvl1 value for each cell.

The fourth method is slightly different as it accounts for both the minima and maxima. The equation used is presented below.

$$SM_i = \frac{N_i - N_{min}}{N_{max} - N_{min}} (swvl1_{max} - swvl1_{min}) + swvl1_{min} \quad (8)$$

That is, for each cell, the SM value is obtained based on the N value's relative position within the minimum and maximum values of N, considering the minimum and maximum values of swvl1 for that cell. This allows the obtained SM values to align fully within the range of swvl1 values; i.e., in the range of [$swvl1_{min}$, $swvl1_{max}$].

3.1.2.7. Analysis of SM Estimates using Baseline Irrigation Data

A further analysis was done by relying on irrigation calendar data described in Section 2.7. As shown in Table 4, considering the areas for which calendar data is available, irrigation is spread out evenly over the

different days of the week, with around 11-17 % of the areas, in terms of size, being irrigated on each day. Moreover, Figure 3 shows that there aren't any significant clusters of adjacent fields being irrigated on the same day. Given this spatial and temporal distribution, and considering that the SM estimates have a spatial scale of ~1 km, a generalized analysis based on the complete dataset would lack accuracy and representativeness. As a result, a careful selection process was followed to select appropriate cells for the analysis.

Before moving on with the procedure for the selection process, which is mainly based on areal averages, i.e., weighted averages done based on the area covered by each element, it's important to identify the different areas considered. The first area considered is the cell size, A_{CELL}, which for the case of the considered target grid, would be 250,000 m^2 (500 x 500 m). The second area, A_{AGRI}, represents all the agricultural fields the lie within a grid cell. The third area, $A_{AGRI,CAL}$, represents all the agricultural fields within a grid cell that have irrigation calendar data. Consequently, $A_{AGRI,ND}$ represents all the agricultural fields within a grid cell that do not have irrigation calendar data available; these are important to consider as these areas were used to obtain the SM estimates and. As a result, their impact on the SM values should be considered. Finally, A_{MON}, A_{TUE},…,A_{SUN} represent the agricultural areas within a grid cell that are aggregated on Monday, Tuesday, …, Sunday respectively. In this context,

$$A_{AGRI} = A_{AGRI,CAL} + A_{AGRI,ND} \tag{9}$$

$$A_{AGRI,CAL} = A_{MON} + A_{TUE} + \cdots + A_{SUN} \tag{10}$$

In this regard, first, the cells which didn't contain any fields with known irrigation calendars were filtered out. Then, the following calculations were done, cell-by-cell, for all cells that were kept after this filtering.

Then, the percentage of agricultural areas within a cell were calculated based on the equation below.

$$A_{AGRI,\%} = \frac{A_{AGRI}}{A_{CELL}} \tag{11}$$

Then, this was used to calculated "weights" for each day of the week (DOW), as follows:

$$W_{DOW} = \frac{A_{DOW}}{A_{AGRI}} \tag{12}$$

Another weight was also calculated to account for the irrigated areas that lie within a cell but do not have calendar data.

$$W_{ND} = \frac{A_{AGRI,ND}}{A_{AGRI}} \tag{13}$$

The weights, then, represent the percentage of agricultural areas that are either irrigated on a specific day of the week, or, in the case of W_{ND}, that do not have calendar data.

For a cell to be considered in the analysis, it has to preferably satisfy two conditions: first, a significant part of it should be covered by agricultural areas, meaning that it should have a high $A_{AGRI,\%}$ and, second,

a significant part of that agricultural area should have irrigation calendar data, meaning that it should have a low W_{ND}.

3.2. The SM-based Inversion Approach

3.2.1. Theoretical Background

The SM-based inversion approach uses as a starting point SM2RAIN, an algorithm originally developed to estimate rainfall amounts from soil moisture data (Brocca et al., 2015, 2016, 2017). As described by Brocca et al. (2018), it considers the soil water balance equation, expressed by:

$$nZ\frac{dS(t)}{dt} = r(t) + i(t) - g(t) - sr(t) - e(t) \quad (14)$$

where n [-] is the soil porosity, Z [mm] is the soil layer depth, S(t) [-] is the relative saturation of the soil or relative soil moisture, t [days] is the time, r(t) [mm/day] is the rainfall rate, i(t) [mm/day] is the irrigation rate, g(t) [mm/day] is the drainage (deep percolation plus subsurface runoff) rate, sr(t) [mm/day] is the surface runoff and e(t) [mm/day] is the actual evapotranspiration.

The equation itself is simple, relating the change in soil moisture in a given soil layer, to five parameters, in the form of two sources (rainfall and irrigation) and three sinks (drainage, surface runoff, and actual evapotranspiration). As can be seen above, the equation contains six terms in total: one term on the left and five terms on the right side. With the irrigation value being the target/output variable, the remaining four parameters, in addition to the soil moisture variations, would be needed as input. This forms the basis upon which all further studies using this algorithm were done. In this context, the main difference between the various studies adopting this approach is how each of the five input parameters is represented and the sources of data used to obtain these values.

Some modifications are done to Equation (14) before proceeding with the algorithm. First, the product between the soil porosity, n, and the soil layer depth, Z, is alternatively represented as one term, Z* [mm], to indicate the soil layer's water capacity. Second, the terms representing the two water sources, irrigation and rainfall, are merged into one term that accounts for all "input" water, represented by W_{in}, as shown in the equation below.

$$Win(t) = r(t) + i(t) \quad (15)$$

This term, which will be the algorithm's main output, is then placed on the left side of the soil water-balance equation, with all other terms on the right side. Consequently, Equation (14) becomes as follows:

$$Win(t) = Z^*\frac{dS(t)}{dt} + g(t) + sr(t) + e(t) \quad (16)$$

Surface Runoff, sr(t)

It has been shown that the portion of water that disperses as surface runoff is negligible and isn't very influential in the algorithm's estimations (Brocca et al., 2015; Jalilvand et al., 2019). In this context, the term representing surface-runoff, sr(t), is neglected and thus dropped from the equation.

Drainage, g(t)

Famiglietti and Wood (1994) demonstrated the strong effect of soil moisture on flows of mass and energy between the atmosphere and the ground surface. They suggested, based on this idea, to estimate the drainage term from soil moisture using the power law. This was adopted in several studies since then (Brocca et al., 2014; Jalilvand et al., 2019; Dari et al., 2020,2022,2023), utilizing the following equation to link the two terms:

$$g(t) = aS(t)^b \tag{17}$$

where a [mm/d] and b [-] are drainage parameters, representing the non-linear relationship between soil moisture and drainage.

Evapotranspiration, e(t)

Regarding the evapotranspiration term, its contribution was assumed to be negligible in the first few use cases of SM2RAIN (Brocca et al., 2015). Since then, various relations relating it to soil moisture and the potential evapotranspiration have been used. In Brocca et al.'s study of 2018, evapotranspiration (ET) was estimated linearly from the potential evapotranspiration (PET), as follows:

$$e_s(t) = PET(t) \times S(t) \tag{18}$$

where PET was estimated using the empirical relation of Blaney and Criddle as modified by Doorenbos and Pruitt (1977):

$$PET_{DP}(t) = K_c\,\{-2 + 1.26[(0.46T_a(t) + 8.13)]\} \tag{19}$$

Where $T_a(t)$ [°C] is the air temperature and K_C [-] is a correction factor.

In Dari et al. (2020), ET was calculated in two different ways. For the calibration of the algorithm, which only considers days with rainfall (when there is theoretically no water stress), Equation (18) was used to get ET from PET. This is mainly due to the nature of the areas chosen for this step. The chosen areas for calibration were drylands surrounding the agricultural areas of concern; in this context, given that, in drylands, evaporation dominates over transpiration, Equation (18) was deemed appropriate. PET, referenced in the equation below as PET_{PM}, was obtained using the method of FAO Penman-Monteith (1998):

$$PET_{PM}(t) = \frac{0.408\Delta(R_n - G) + \gamma \frac{900}{T + 273} u_2(e_s - e_a)}{\Delta + \gamma(1 + 0.34u_2)} \tag{20}$$

where Δ [kPa/°C] is the slope of the vapor pressure curve, R_n [MJ/m^{2}day] is the net radiation at the crop surface, G [MJ/m^{2}day] is the soil heat flux density, T [°C] is the mean daily air temperature at 2 m height, u_2 [m/s] is the wind speed at 2 m height, e_s [kPa] is the saturation vapor pressure, e_a [kPa] is the actual vapor pressure and γ [kPa/°C] is the psychrometric constant.

Equation (20) "was obtained from the original Penman-Monteith equation and refers to a terrestrial surface characterized by a standard grass crop of 12 cm height, a fixed surface resistance of 70 s/m, and a fixed albedo equal to 0.23" (Dari et al., 2020). The study relied on four variables, namely the solar radiation, wind speed, air temperature, and air's relative humidity, to infer all the required parameters in the equation.

For the step of irrigation estimations, however, which considers agricultural areas (rather than drylands), using Equation (18) would undermine the contribution of transpiration to ET. As a result, the FAO's dual

crop coefficient approach, suggested in the study of Allen et al. (1998), was adopted. This method comprises of getting ET as the product between PET and the crop coefficient, K_C [-], as follows:

$$e_{FAO}(t) = PET(t) \times K_c \tag{21}$$

where the crop coefficient is basically the sum of the transpiration from the crop and the evaporation from the soil:

$$K_c = K_{cb} + K_e \tag{22}$$

where transpiration is represented by the basal crop coefficient, K_{cb} [-], and evaporation is represented by the soil water evaporation coefficient, K_e [-]. Furthermore, to account for limited water availability, the transpiration term is multiplied by the water stress coefficient, K_s [-]:

$$K_c = K_s K_{cb} + K_e \tag{23}$$

Dari et al. (2022) compared the performance of the SM-inversion algorithm considering different methods to obtain the evapotranspiration, in their comprehensive study over a 10,000 km^2 area in Spain, surrounding the Ebro basin. For the calculation of the potential evapotranspiration, the authors considered three options. The first option was Penman-Monteith, represented by Equation (20). The second option was the formula suggested by Hargreaves (Hargreaves and Samani, 1982, 1985):

$$PET_H = 0.0023(T + 17.8)(T_{max} - T_{min})^{0.5} R_a \tag{24}$$

where T_{min} [°C], T [°C], and T_{max} [°C] are the minimum daily temperature, mean daily temperature, and the maximum daily temperature (for a specific day, measured at 2m height) respectively, and R_a [MJ/m^{2}day] is the extraterrestrial radiation.

One possible equation to calculate Ra, proposed by Duffie & Beckman (2013), and later presented and summarized clearly by Machairas (2022) is presented below.

$$Ra = \frac{1440}{\pi} G_s d_r [\omega_s \sin(\phi) \sin(\delta) + \sin(w_s) \cos(\phi) \cos(\delta)] \tag{25}$$

Where

$$d_r = 1 + 0.033 \cos\left(\frac{2\pi}{365} J\right),$$
$$\delta = 0.409 \sin\left(\frac{2\pi}{365} J - 1.39\right), \textit{ and}$$
$$\omega_s = \arccos[-\tan(\phi) \tan(\delta)]$$

In Equation (25) and its related formulas, G_s [0.082 MJ/m²/d] is the solar constant, d_r [-] is the inverse relative distance from the Earth to the sun, δ [rad] is the solar declination angle, ω_s [rad] is the sunset hour angle, Φ [rad] is the geographical latitude, and J [1 to 365 or 366] is the day of year.

The third option was to directly retrieve PET values from MODIS observations, namely the MOD16A2, which is a product that relies on the MODIS16 ET processing algorithm, which in turn is based on the Penman-Monteith formula, presented in Equation (20).

Considering the above three options for obtaining PET, the study additionally considered two alternative ways to relate ET to PET. The first method, named as "SM-limited" method, consisted of adopting Equation (18), which considers the relative soil moisture to relate the two terms. The second method, named as "FAO56" method, relied on Equation (21) which relates ET to PET via the crop coefficient K_c instead.

In this context, three methods to obtain PET (Penman-Monteith, Hargreaves, and MODIS) combined with two methods to get ET from PET (SM-limited or FAO56) yields six test cases. It should be noted that, in all six cases, the SM-limited method was used in the calibration step, in accordance with Dari et al. (2020), with the reason being the use of drylands for calibration. The choice of using the SM-limited or the FAO56 approach to derive ET from PET only applies to the step of irrigation estimation.

Furthermore, one additional case, which directly considers the ET data derived from MODIS observations, was also added to make it a total of seven configurations considered in the study. This direct retrieval of ET data instead of obtaining PET and then relying on additional data to estimate ET from PET makes the seventh configuration as one representing additional reliance on remote sensing data.

The study relied on the Budyko framework to cross-check results obtained by the algorithm and compared the performance of the seven configurations by considering the 5-day aggregated results via several metrics, namely The Kling-Gupta efficiency (Gupta et al., 2009), the Pearson correlation coefficient (r), the percent bias (PBIAS), and the root mean square error (RMSE). It should be noted that, for the former two coefficients, higher scores indicate a better result, as opposed to the latter two coefficients, where low scores indicate a better performance.

In summary, the authors were able to draw out three main conclusions from that study (Dari et al., 2022). First, the use of meteorological data to compute PET, combined with the adoption of the SM-limited approach to get ET from PET, is not recommended as it largely neglects the transpiration component of ET, and thus doesn't account for the significant impact of vegetation on ET. Second, the use of the Hargreaves formula within the FAO56 approach was deemed a viable alternative to the more thorough and computationally-intensive Penmen-Monteith equation as they were shown to yield comparable results on all the considered performance metrics. Third, the computation of irrigation estimates using only remote sensing data was shown to have promising potential, which justifies the investment of more effort into optimizing and improving approaches such as the seventh case considered in the study.

More recently, in the study of Dari et al. (2023), a different method to compute ET was proposed. In that study, PET data was obtained from Global Land Evaporation Amsterdam Model (GLEAM) v3.5b product. Due to the coarse resolution of the adopted PET data, they computed ET as the product of PET, SM, and an adjustment factor F, leading to the formula below:

$$e_F(t) = PET \times S(t) \times F \tag{26}$$

The adjustment factor, F [-], can range between 0.6 and 1.4 and is intended to account for uncertainties in the ET estimates (Modanesi, 2021).

This study relies on Hargreave's formula (Equation (24)) to calculate PET, and on Equation (26) to obtain ET from PET.

Soil Moisture, S(t)

Given that the variation in soil moisture is the basis of the soil water balance equation, displayed in Equation (14), and that soil moisture is needed to obtain both the drainage and the evapotranspiration components, the reasoning behind naming the approach the "SM-inversion approach" is evident. In this context, unlike the other parameters, soil moisture estimates are obtained independently, from remote sensing data. Early studies, namely that of Brocca et al. (2018), relied on coarse resolution data from four different missions/sensors: SMAP (Soil Moisture Active Passive), SMOS (Soil Moisture and Ocean

Salinity), ASCAT (Advanced SCATterometer), and AMSR2 (Advanced Microwave Scanning Radiometer 2). Some relevant information about the missions is displayed in the table below.

Table 6 - Coarse-resolution radar sensors/missions for soil moisture estimation (evaluated by Brocca et al., 2018)

Mission Name	Acronym	Launch Date	Instrument Description	Spatial Resolution [km]	Revisit Period [days]	Source
Soil Moisture Active Passive	SMAP	2015	Active and passive L-band microwave sensors[1]	36	3	Entekhabi et al., 2010
Soil Moisture Ocean Salinity	SMOS	2009	L-band microwave radiometer	40	3	Kerr et al., 2001
Advanced SCATterometer	ASCAT	2006/2012	C-band scatterometer	25	1	Wagner et al., 2013
Advanced Microwave Scanning Radiometer 2	AMSR2	2012	Multi-frequency radiometer	25	2	Owe et al., 2008

[1]the active sensor experienced failure, causing studies to rely on data solely from the passive sensor

Given the limitations faced due to the coarse resolution of the soil moisture data, the next attempt at improving the method comprised of downscaling the soil moisture data to a spatial resolution of 1 km, most commonly via the DISaggregation based on Physical And Theoretical scale Change (DISPATCH) method, initially proposed by Merlin et al. (2013) (Dari et al., 2020, 2022).

This study, however, relies on an alternative approach to get soil moisture, presented more recently by Dari et al. (2023). In that study, soil moisture data was obtained from Sentinel-1 images via the RT1 model (Section 3.1).

SM Noise Reduction Through Exponential Filter

Albergel et al. (2008) proposed the use of an exponential filter, originally published by Wagner et al. (1999), to diminish noise from soil moisture data. Their method considers that the soil moisture obtained from radar observations is the surface soil moisture, and, consequently, relies on a simplified two-layer water-balance approach in an attempt to estimate root-zone soil moisture from remotely-sensed soil moisture values. The corrected soil moisture measures, which are referred to as Soil Water Index (SWI), can be computed using the iterative formulas shown below (Stroud, 1999).

$$SWI_{m(n)} = SWI_{m(n-1)} + K_n\left(S(t_n) - SWI_{m(n-1)}\right) \quad (27)$$

Where $SWI_{m(n)}$ [-] is the corrected soil moisture measure for a radar acquisition n, taken at a time, t_n, $S(t_n)$ [-] is the initial, uncorrected SM estimate for the same acquisition n, K_n [-] is the "gain" factor, also at time t_n, and $SWI_{m(n-1)}$ [-] is the corrected soil moisture measure for the preceding radar acquisition, n-1.

The iterative formula to calculate the gain factor is presented below.

$$K_n = \frac{K_{n-1}}{K_{n-1} + e^{-\frac{t_n - t_{n-1}}{T}}} \quad (28)$$

Where K_{n-1} is the gain factor of the preceding radar acquisition, n-1, taken at a time, t_{n-1}, and T [days] is the characteristic time length. Considering the expected timescale of gaps between consecutive radar acquisitions, the difference from subtracting the two acquisition times is also expressed in days.

T, being the only parameter on which this approach is based, is intended be a proxy for all the factors that influence the temporal dynamics of SM, such as run-off, evaporation, soil thickness, and relevant soil characteristics, such as density or hydraulic conductivity.

The study analyzed the impact of some of these influential factors. It was shown that T gives an idea about a soil's response time, as it increases with increasing soil depth/thickness considered for SM measurements; additionally, larger T values are obtained for areas with high temperature and wind (Albergel et al., 2008). On the other hand, T appeared to be insensitive to soil characteristics.

Using this exponential filter to reduce noise in SM estimates seems to be common practice as it's been adopted in several studies (Brocca et al., 2014, 2016, 2017, 2018; Bauer-Marschallinger, 2019). Although it was initially intended to reduce noise from low-resolution SM datasets such as SMAP, SMOS, and ASCAT, it was more recently used by Dari et al. (2023) who dealt with higher-resolution SM data, and, therefore, an attempt to consider it was also included in this study. Moreover, since the choice of its parameter T is not elaborated in the mentioned studies, the inclusion of this filter assumes an approach similar to a previous study done by Brocca et al. (2016), where the parameter T was fitted along with the rest of the model parameters.

Definition of Cost Function and Method for Fitting Procedure

Since the algorithm was first proposed by Brocca et al. (2014), the fitting procedure adopted to calibrate the unknown parameters has varied and developed across studies. This difference can be attributed to several factors, such as the availability of reference irrigation data, the characteristics of soil moisture data used as input, and the diverse methods used to represent and correct evapotranspiration.

However, despite their differences, the adopted cost function for all methods was RMSE where the error is the difference, for each row of data, between the modelled and observed water input, as shown in the equation below.

$$RMSE = \sqrt{\sum\left(W_{in,measured} - W_{in,modeled}\right)^2} \tag{29}$$

Brocca et al. (2018)'s method had four unknown parameters to be calibrated. They relied on Equation (19) to estimate ET from PET. They relied on scatterometer data, which allowed them to work at a daily timescale. Their approach consisted of calibrating all the unknown parameters simultaneously to directly obtain irrigation estimates. Since the irrigation volumes are unknown, they considered only days with rainfall for the calibration, based on the assumption that irrigation on these days would be zero. The parameters were, then, calibrated, considering only this subset of data, to minimize the RMSE. The obtained daily estimates of irrigation were then aggregated to the monthly timescale. The monthly amounts that were less than 1.5 times the monthly irrigation were considered insignificant and consequently masked out. Finally, negative irrigation values and all irrigation during the winter periods were also masked out. A summary of this procedure, taken directly from Brocca et al. (2018), is presented below.

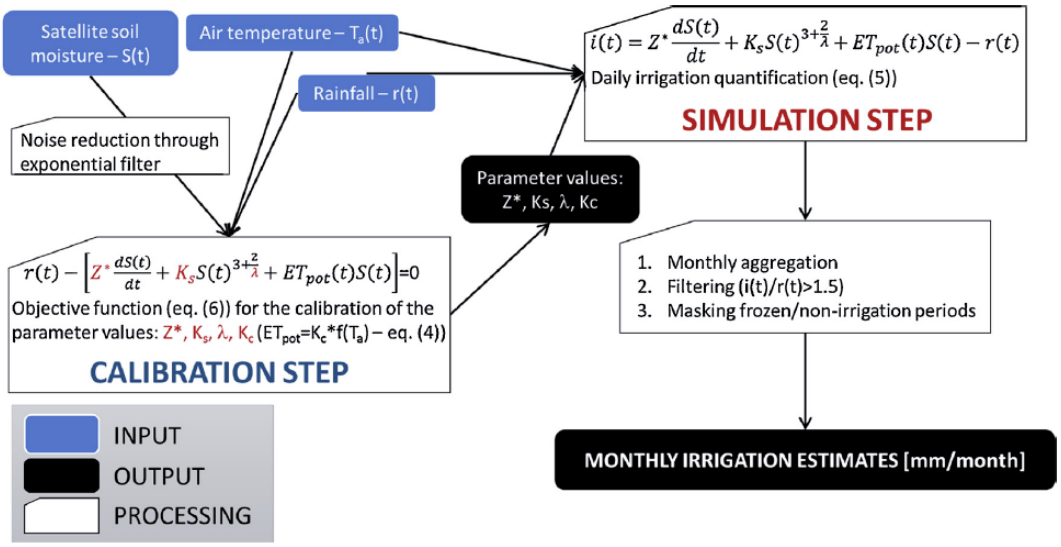

Figure 8 - Summary of fitting procedure adopted in Brocca et al., 2018 (source: Brocca et al., 2018)

Dari et al. (2020), as previously mentioned, chose to do the calibration over drylands close to their agricultural area of interest. This meant that they wouldn't have to worry neither about irrigation nor transpiration, which allowed them to do the calibration for just 3 parameters, and without the need for reference irrigation data. They, then, used the median values as fixed parameters to estimate the total water input, W_{in}. They were also able to obtain results at a daily timescale due to their reliance on scatterometer data. After that, they subtracted rainfall rates from the W_{in} estimates to get irrigation estimates, masked out negative irrigation values, and aggregated the daily results to a 5-day interval. A summary of this procedure, taken directly from their study, is presented below.

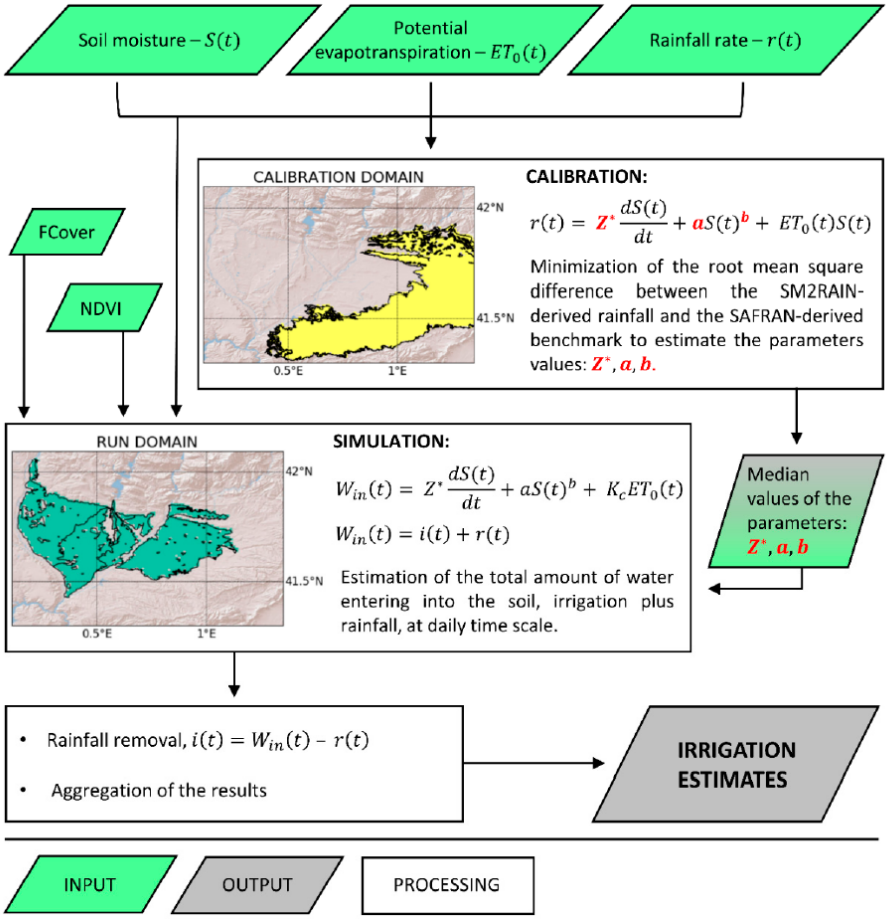

Figure 9 - Summary of fitting procedure adopted in Dari et al., 2020 (source: Dari et al., 2020)

As previously mentioned, the more recent study of Dari et al. (2023), adopted an alternative approach proposed by Modanesi (2021) (Equation (26)) to obtained ET from PET. This approach introduced an additional parameter, F, to the fitting, which led them to rely on an iterative fitting procedure instead. A summary of this procedure, taken directly from their study, is presented below.

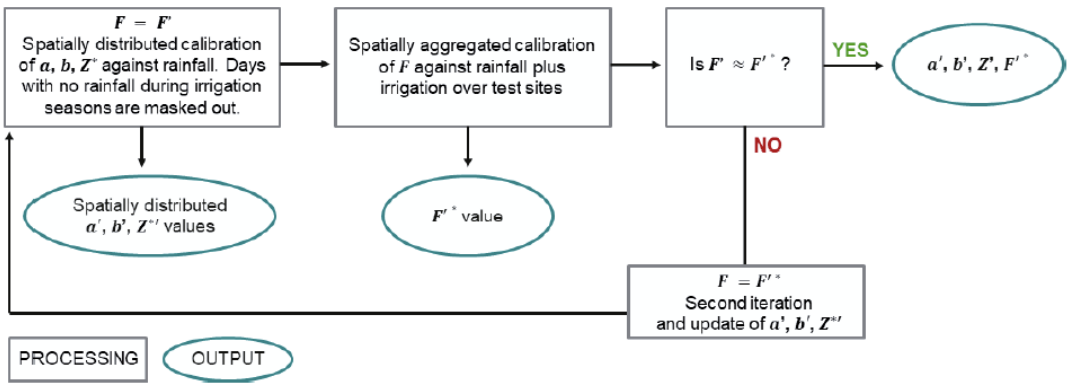

Figure 10 - Summary of iterative fitting procedure adopted in Dari et al., 2023 (source: Dari et al., 2023)

The parameters to be fitted, in their study, were a, b, Z*, and F. Consequently, each fitting iteration consisted of two steps.

In the first step, the value of F was fixed, and only days with rainfall and within the irrigation period were considered to calibrate a, b, and Z*. This was done over the whole area of interest, cell-by-cell, meaning that each cell had its own values of a, b, and Z*. For the first iteration, F was set to 1. For the subsequent iterations, F was set to the weighted average calculated in the second step of the previous iteration.

In the second step, the obtained values of a, b, and Z* from the first part were fixed, and only days with known irrigation volumes were considered to calibrate the value of F. This was done only over regions having baseline irrigation data, region-by-region, meaning that each region had one value for F. Then, the weighted average of F, based on each region's area, was calculated and assumed to represent the whole area of interest.

The fitting ended when the value of F obtained from the second step aligned with the value of F that was used in the first step. Consequently, the values of a, b, Z*, and F, obtained from the fitting, were used to produce estimates of total water entering the soil, W_{in}. Rainfall was subtracted from these W_{in} estimates to obtain irrigation estimates. Then, negative values of irrigation were disregarded. Finally, the weekly irrigation amounts that were less than 20% of the weekly rainfall volume were considered negligible and also disregarded. It should be noted that their outputs were at the weekly timescale since they relied on Sentinel-1 data for SM, as opposed to previous studies that relied on coarse-resolution data available at the daily timescale.

3.2.2. Implementation of SM2Rain Algorithm

Based on the discussion in Section 3.2.1, considering the algorithm's main soil-water balance equation (Equation (16)), then neglecting the surface runoff, sr(t), linking drainage, g(t), to SM (Equation (17)), and considering the approach of Modanesi (2021), which was also adopted by Dari et al. (2023), to obtain the evapotranspiration, e(t), as a product of PET, SM, and a correction factor F (Equation (26)), Equation (16) then becomes as follows.

$$Win(t) = Z^* \frac{dS(t)}{dt} + aS(t)^b + PET \times S(t) \times F \tag{30}$$

Four of the parameters in Equation (30), namely a, b, Z*, and F, are estimated through an iterative fitting procedure. Also, for the cases where the exponential filter is considered, a fifth parameter, T, is also included in the fitting procedure (Brocca et al., 2016). This, however, requires the preparation of soil moisture, S(t), PET, and rainfall, r(t), which is a component of $W_{in}(t)$, data to be used as inputs for the fitting. This is explained in the subsections below.

Similar to the implementation of the RT1 algorithm, all the processing and analysis for the SM-based inversion approach was done using the Python language, through original code, consisting of multiple scripts and functions, developed specifically for the purpose of this study. The processing, presentation, and analysis of this algorithm's results were done with the help of numerous open-source packages, most importantly: xarray (Hoyer et al., 2024), rioxarray (Alan et al., 2024), pyproj (Alan et al., 2023), dask (Rocklin, 2015), numpy (Harris et al., 2020), scipy (Virtanen et al., 2020), pandas (The pandas development team, 2024), matplotlib (Caswell et al., 2024), and geopandas (Bossche et al., 2024).

3.2.2.1. Input Data

Soil Moisture, S(t)

The soil moisture data is obtained via the RT1 approach (Section 3.1).

Two alternative datasets, the one obtained with the maxima-driven scaling and the one obtained with Equation (8) are considered. Apart from the different SM values contained in each dataset, all their other characteristics, including their temporal and spatial resolution and their temporal and spatial coverage are identical. The two scaling methods are explained in detail in Section 3.1.2.4. The differences between the obtained datasets are analyzed in Section 4.1.2.

The SM data initially consists of a timeseries, with irregular time intervals, covering a period of three years, from 2020 to 2022. This time period covered is split into two periods: 2020-2021, when both Sentinel-1 SARs were still operation, and 2022. The first period, of 2020-2021, is used to perform the fitting procedure. On the other hand, the fitting results are applied to produce estimates for the second period, of 2022. Spatially, the data is already filled on the generated target grid with a ~1 km resolution and covering the whole study area of agricultural fields.

In terms of data preparation, two alternatives are considered: keeping the series with irregular time intervals and resampling it into a regular time interval. The interval was chosen based on the largest time gap between consecutive Sentinel-1 observations. Consequently, the smallest interval that could be considered was 12 days, which coincides with Sentinel-1's revisit period over the study's area of interest. The temporal resampling is done by averaging all SM values contained within each 12-day interval. No modifications are needed concerning the spatial aspect since the data is already loaded on the target grid, having the target spatial resolution of the study (~1 km).

This leads to four alternative SM datasets, summarized in the table below, to be used as input for the SM-based inversion algorithm.

Table 7 - Summary of alternative SM datasets considered in the SM-inversion approach

SM Dataset	Scaling method	Temporal Resampling	Time Interval	Spatial Resolution [km]
SM1	Maxima	No	Irregular	~ 1
SM2	Minima and maxima			
SM3	Maxima	Yes	12 days	
SM4	Minima and maxima			

Potential Evapotranspiration, PET

As already mentioned in Section 2.4, PET is calculated using the Hargreaves formula (Equation (24)). The equation relies on temperature data, obtained from ARPA Piemonte's Caluso station, as described in Section 2.5, and extraterrestrial radiation, calculated using Equation (25), based on the latitude and the day of year. The obtained PET data is then in the form of a daily timeseries, displayed in the Figure 11.

Rainfall, r(t)

Daily timeseries of rainfall data, obtained from ARPA Piemonte's Caluso station and presented in mm/d, are displayed, along with the calculated PET data, in the figure below.

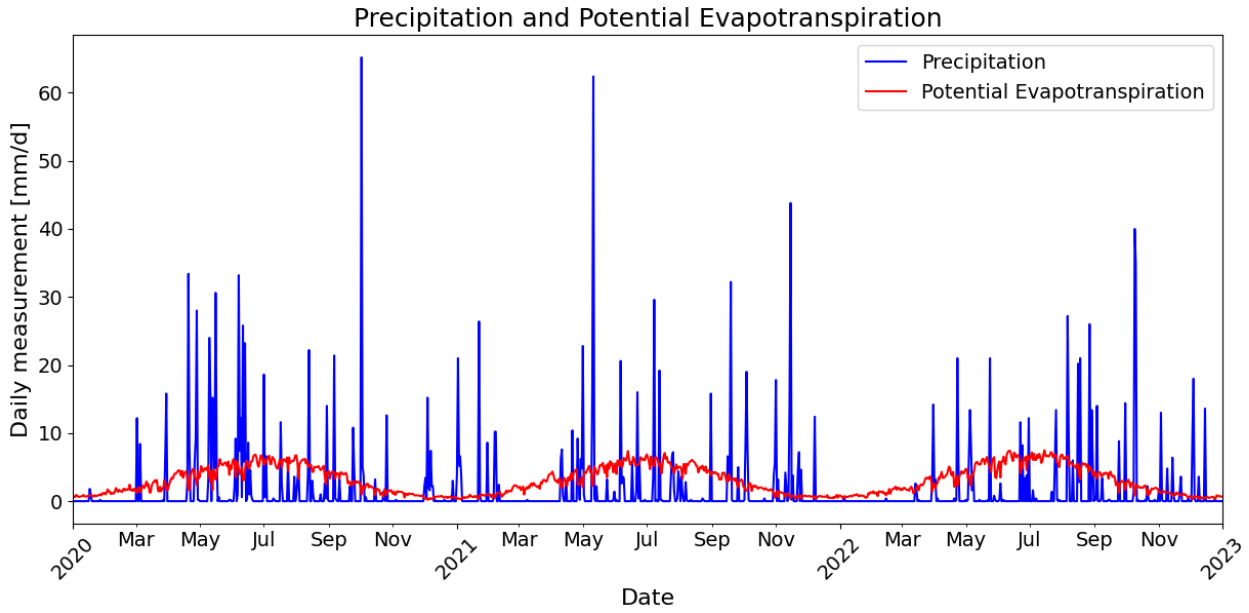

Figure 11 - PET (obtained using Hargreaves) and Precipitation (obtained from Caluso meteo-station) timeseries

3.2.2.2. Temporal Aggregation of P and E Data

The rainfall and evapotranspiration are both available at a daily timescale, while the SM data, whether for the irregular or the resampled timeseries, is not available daily. As a result, it is necessary to aggregate the P and E data based on the entries available for SM. A data template is used to explain how this aggregation is done. All values present in the template below are fabricated for illustrative purposes only.

Table 8 - Data template before aggregation

Row number	Date	E [mm]	SM [-]	P [mm]
1	1/1/2024	1	0.2	101
2	1/2/2024	2	-	102
3	1/3/2024	3	-	103
4	1/4/2024	4	-	0
5	1/5/2024	5	-	105
6	1/6/2024	6	0.5	106
7	1/7/2024	7	0.3	107
8	1/8/2024	8	-	0
9	1/9/2024	9	0.4	0
10	1/10/2024	10	0.35	0

In accordance with Dari et al. (2023), the aggregation is done by summing E and P values from all rows within in a gap of SM data and assigning them to the subsequent date with an SM value. In the case of an irregular timeseries, such as the one displayed in Table 8, the aggregated dataset would look as follows.

Table 9 - Data template after aggregation

Row number	Date	E [mm]	S [-]	P [mm]
1	1/1/2024	1	0.2	101
6	1/6/2024	20	0.5	416
7	1/7/2024	7	0.3	107
9	1/9/2024	17	0.4	0

10	1/10/2024	10	0.35	0

Two gaps were present in the data from Table 8, a gap from row 2 to row 5 and another at row 8. Consequently, as shown by the aggregated results in Table 9, row 6 was assigned the total E and P for rows 2 to 6, while row 9 was assigned the total E and P for rows 8 to 9. In contrast, rows 1, 7, and 10 kept only their respective data since they were not preceded by any gaps.

It should be noted that the aggregated dataset, in the case of the template given, consists of just five rows; the old row numbers (1, 6, 7, 9, 10) were kept only as a reference to the initial template.

In the case of resampled data, this aggregation would mean that in all rows after the first one, the E and P values represent the total E and P that took place within the 12-day period leading up to that row's date.

3.2.2.3. Incorporation of dS, dt, I, and W into Input Dataset

After obtaining the required input data of rainfall, evapotranspiration, and soil moisture, the calculation of some additional variables present in Equation (30) is done as a final step before proceeding with the fitting attempts. Considering the same template described above, the dataset becomes as follows.

Table 10 - Aggregated data template prior to fitting

Row number	Date	E [mm]	S [-]	P [mm]	I [mm]	Win_measured [mm]	dS [-]	dt [days]
1	1/1/2024	1	0.2	101	0	101	0	1
6	1/6/2024	20	0.5	416	0	416	0.3	5
7	1/7/2024	7	0.3	107	0	107	-0.2	1
9	1/9/2024	17	0.4	0	0	0	0.1	2
10	1/20/2024	10	0.35	0	0	0	-0.05	1

I, representing irrigation, is initialized to 0 for the time being. This is explained in the following subsections discussing the fitting procedure.

$W_{in,measured}$ is the sum of rainfall and irrigation measurements (Equation (15)).

For the first row, dS is set to 0. For subsequent rows, it is calculated as the difference in soil moisture, S, between each row and the row preceding it.

For the first row, dt is set to 1. For subsequent rows, it is calculated as the time difference, in days, between each row and the row preceding it.

3.2.2.4. Fitting/Calibration of Model Parameters

The approach considered in this study for the calibration of model parameters is mostly similar to that adopted by the most recent study of Dari et al., 2023; it has notable differences, nonetheless, which are elaborated below.

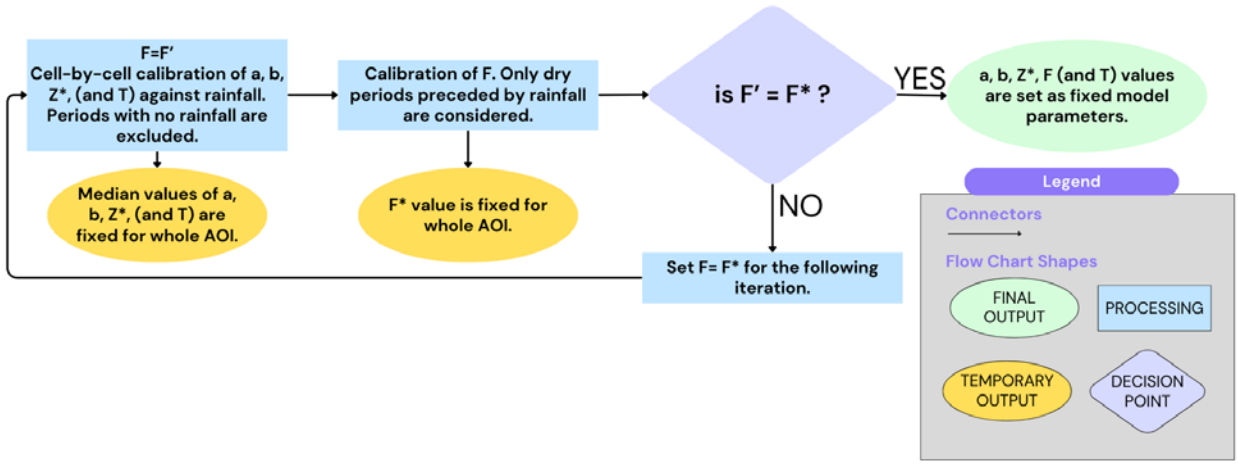

Figure 12 - Summary of iterative fitting procedure adopted in this study

Two alternative fitting procedures were tested. In the first alternative, the parameter T, required to apply the exponential filter, is calibrated in the first step, along with a, b, and Z*, in accordance with Brocca et al., 2016. In the second alternative, the exponential filter was not applied; as a result, the fitting was done just for a, b, Z*, and F. Consequently, both fitting alternatives were repeated for each of the four SM datasets considered (Table 7), using only the data from the period of 2020-2021.

For the procedure without the exponential filter, the SM values for each dataset were directly used as input for Equation (30) to calculate the modeled W_{in}. In contrast, for the case where the exponential filter is considered, the "corrected" soil moisture results, obtained from applying Equation (27), were placed in Equation (30) instead. The remainder of the fitting procedure is the same for both alternatives.

As suggested by Dari et al. (2023), each iteration is split into two steps: the first step where F is fixed and the remaining parameters are fitted cell-by-cell, and a second step where the other parameters are fixed and F is calibrated.

For the first step, only periods with rainfall are considered. With regards to the template dataset presented in Table 10, this would be the equivalent to considering only rows 1, 6, and 7. In these periods, it is assumed that there would be no need for irrigation, so irrigation values are set to 0 and consequently $W_{in,measured}$ would be equal to the rainfall. For the first iteration, F was set to a starting value of 1; this is represented by F' in Figure 12. This step would, then, by produce, for each cell, values for a, b, Z*, and, optionally, T, that would minimize the RMSE. Considering the relatively small spatial scale over which the study's area of interest extend, these parameters were assumed to not vary significantly throughout the area. As a result, the median values were set as fixed parameters and considered to be representative of the whole AOI.

In the second step, due to lack of baseline irrigation volumes to base the fitting of F on, an alternative consideration was made. The periods that didn't have rainfall, but happened to be preceded by a period with rainfall, were used for the calibration of F. With regards to the template dataset presented in Table 10, this would be the equivalent to considering row 9. This was done considering that, out of all the encountered period without rain, these periods would be the least likely to require irrigation since they directly follow a rainy period. In this step, one value of F is calibrated for the whole AOI. The calibrated value of F obtained from this second step, represented as F* in Figure 12, is then compared to F', which was used in the first step of the iteration. If the difference between the F value used in the first step of an

iteration, F', and the F value obtained from that iteration's second step, F*, is less than 0.01, the values were considered to converge.

As a result, if F' and F* do not converge, another iteration is done, with the F' in the new iteration being set to F* computed in the iteration preceding it. When convergence is reached, the ultimate iteration's parameters are then considered as final and are fixed, thus ending the calibration procedure. It should be noted that fitted parameters can only take on positive values. As a result, all parameters were bounded by a lower limit of 0, except for T, which was limited by 0.01 since it's present in the denominator, to avoid a division-by-zero error.

Since four SM datasets were considered, and two alternative fitting procedures were tested for each SM dataset, the outputs from this step are eight sets of model parameters in total. Expanding on Table 7, the calibration attempts can be summarized as follows.

Table 11 - Summary of model calibration attempts done in SM-based inversion algorithm

Fitting Attempt	Fitting Procedure	SM Dataset	Scaling Method Used to Obtain SM	Temporal Resampling	Time Interval	Spatial Resolution [km]
FA1	Without Exponential Filter (fitted parameters are a, b, Z*, and F)	SM1	Maxima	No	Irregular	~ 1
FA2		SM2	Minima and maxima			
FA3		SM3	Maxima	Yes	12 days	
FA4		SM4	Minima and maxima			
FA5	With Exponential Filter (fitted parameters are a, b, Z*, T, and F)	SM1	Maxima	No	Irregular	
FA6		SM2	Minima and maxima			
FA7		SM3	Maxima	Yes	12 days	
FA8		SM4	Minima and maxima			

3.2.2.5. Calculation of Irrigation Estimates

Each set of calibrated parameters was then analyzed, and when deemed suitable, was used to produce irrigation estimates for the period of 2022. It should be noted that irrigation estimates were produced using the same SM dataset that was adopted to obtain the model parameters. That is, in all cases, the 2022 SM data to produce irrigation estimates would be obtained from the same SM dataset whose 2020-2021 data was used to fit the model.

The estimation was done by replacing the obtained values for a, b, Z*, F, and, optionally, T, in Equation (30), along with the input data of S and E, to calculate W_{in} values. Then, rainfall would be subtracted from the W_{in} values (Equation (15)), to derive irrigation estimates. Similar to previous studies, the negative irrigation estimates were disregarded. At this point, if the dataset isn't already resampled to a 12-day time interval, the irrigation estimates would be aggregated to this regular timescale. Finally, for each 12-day period where the ratio between the irrigation estimates and that period's rainfall was less than 0.2, the irrigation estimates would also be disregarded. This was done, in accordance with Dari et al. (2023), "to remove negligible irrigation amounts attributable to random errors".

4. RESULTS AND DISCUSSION

4.1. RT1

4.1.1. Correlation Between N and Baseline Soil Moisture

In accordance with Quast et al. (2023), the Pearson correlation metric was used to determine the agreement between the RT1 results and the baseline soil moisture reanalysis data. More specifically, the correlation was found, for each cell in the target grid, between the obtained parameter, N (before scaling to SM values), and the baseline soil moisture data, swvl1, obtained from Muñoz Sabater (2019). The results of this analysis are displayed in the form of a map to get an idea about the spatial distribution of the Pearson correlation coefficients, and an empirical probability density function (PDF), to get a better idea about the numerical distribution of these results.

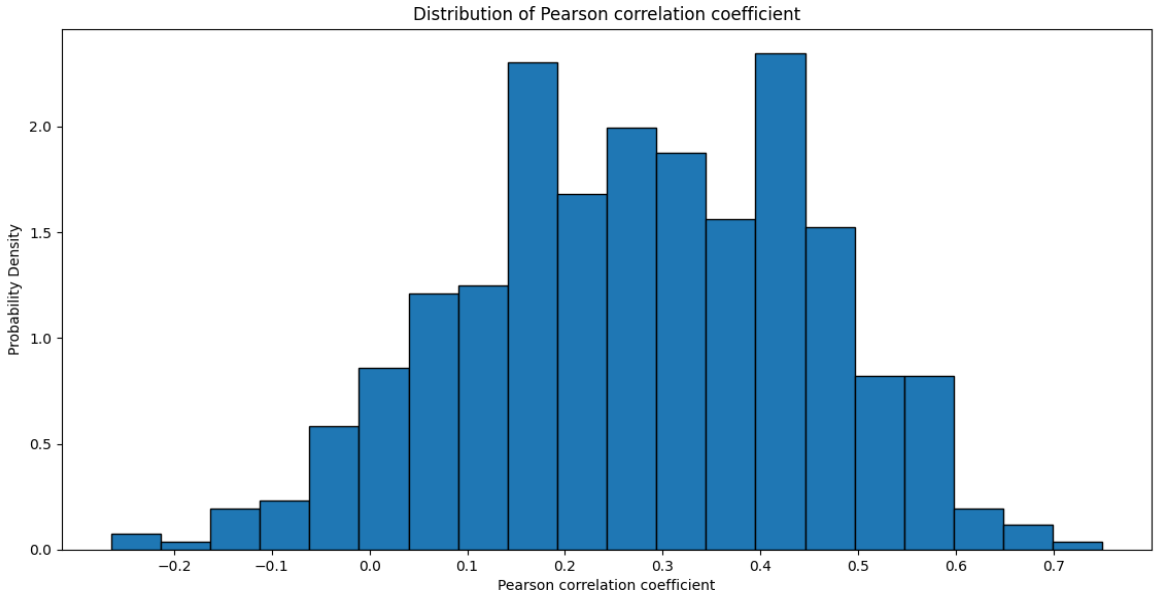

Figure 13 - Density plot of Pearson correlation for RT1 results – per period

It can be seen that the correlation results, when the whole 2020-2023 period is considered, aren't very satisfactory, with a mean of 0.28 and a standard deviation of 0.18.

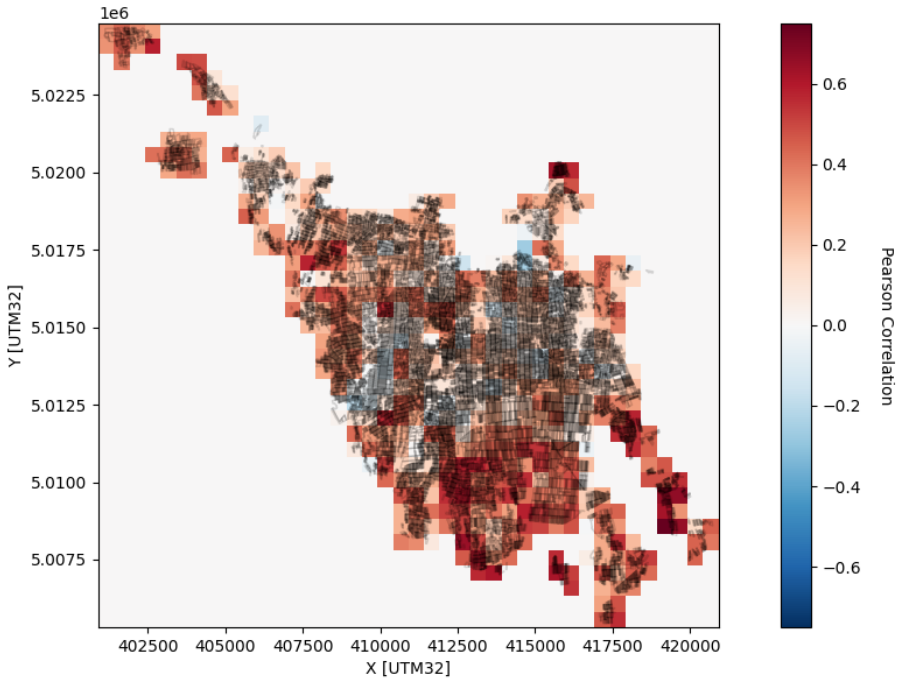

Figure 14 - Spatial distribution of Pearson correlation for RT1 results

The map shows that correlation seems of poorer quality near the center of the figure, with better results overall near the top and the bottom of the AOI. Given that 2022 had approximately half the acquisitions per year compared to 2020-2021, when Sentinel-1B was still operational, the analysis was repeated for each these two periods separately.

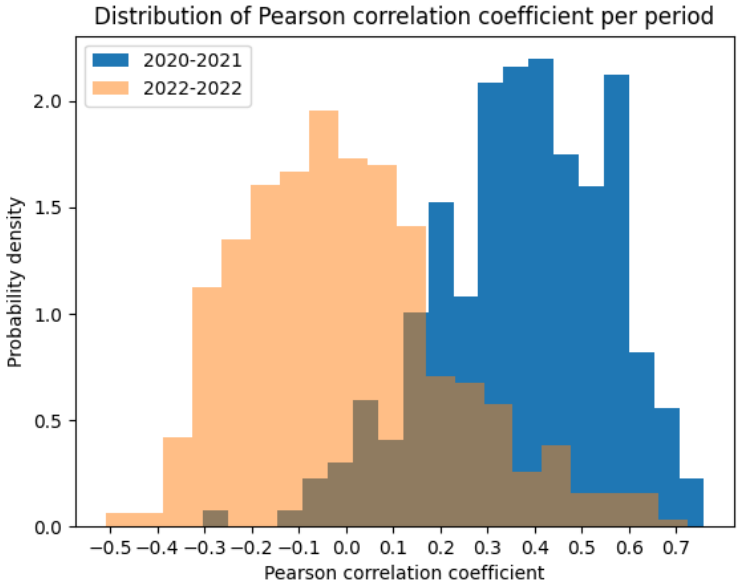

Figure 15 - Density plot of Pearson correlation for RT1 results – per period

This temporal split gives a very different idea, as it shows improved results for the period 2020-2021, with a mean of 0.37 and standard deviation of 0.18. On the other hand, the performance for 2022 is significantly worse, with a mean of 0.0 and a standard deviation of 0.22. Considering that the same data

sources and methodology were used to obtain the N parameter for both periods, in addition to the short time scale at which soil moisture variations occur, this stark difference can be largely attributed to the lower frequency of radar data in the latter period.

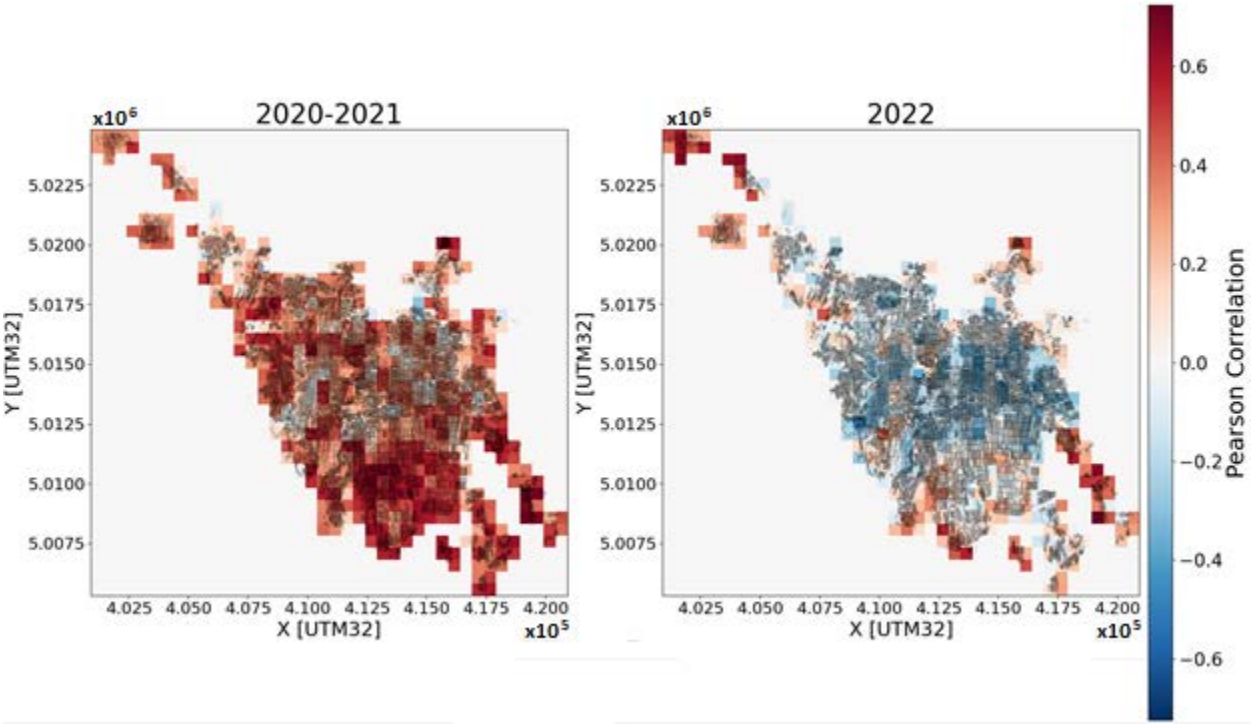

Figure 16 - Spatial distribution of Pearson correlation for RT1 results - per period

The slight difference in correlation results between the center and the bottom and top areas can still be seen, even after the period split. Knowing that several SAR images do not cover the whole AOI (Figure 7), one explanation for this could be the possibility that some areas are covered by more images than others, thus allowing for better retrieval. As a result, a deeper investigation to check the number of images covering each area was done.

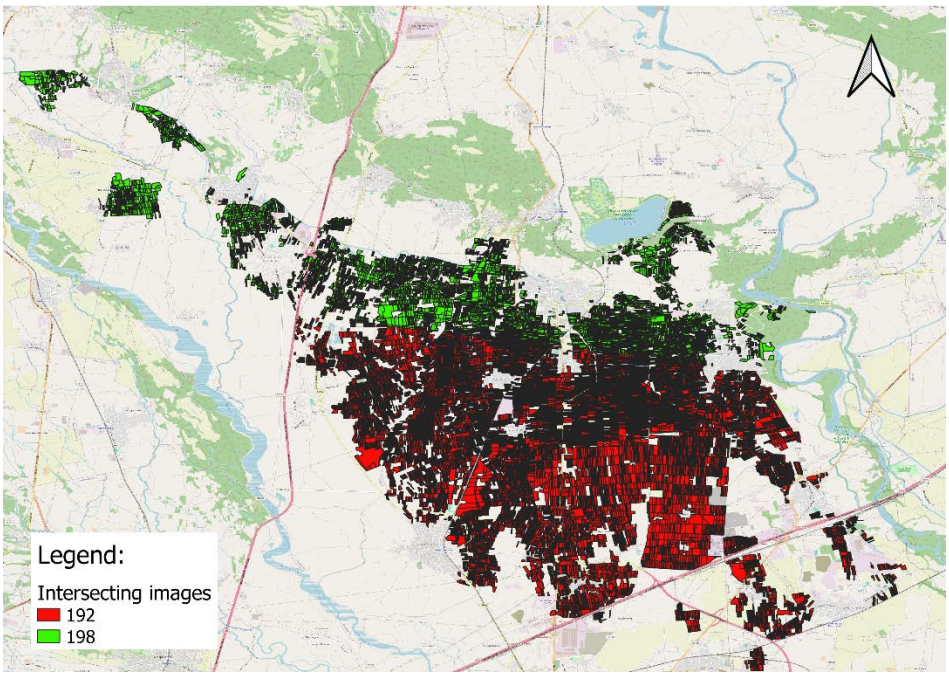

Figure 17 – Map showing the number of SAR images intersecting the agricultural areas (using QGIS and OpenStreetMap)

As the figure above shows, all the agricultural fields in the AOI are covered by approximately the same number of images, with only a small portion at the top being covered by a few extra images. Nonetheless, this difference is not significant and does not justify why some areas at the bottom of the AOI would have slightly better results.

In addition to that, despite this difference being less prominent for the period of 2020-2021, its presence for both periods suggests that the reason behind it is not necessarily time-dependent. One possible explanation could be inaccuracies in the shapefiles chosen to represent the agricultural areas; in other words, some areas near the center might be mistakenly represented as agricultural areas.

Finally, since one option for the SM-based inversion approach was to consider SM results resampled to a 12-day regular time interval, the correlation results obtained after resampling were also considered. The analysis showed that resampling had very little impact on correlation with the baseline SM data. This is shown in Figure 22 and Figure 23 in Appendix A.

4.1.2. Comparison of Scaling Methods from N to SM

As discussed in Section 3.1.2.4, four alternatives were considered to scale from the parameter, N, calibrated through model fitting, to SM. A summary of the four datasets is presented below.

Table 12 - Summary statistics for swvl1 and the four SM datasets

Dataset	Minimum Value	Maximum Value
Smax	0.05	0.51
Smin	0.20	2.19
Smean	0.09	1.17
Sminmax	0.20	0.51
swvl1	0.20	0.51

The scaling attempts done based on the minima and the mean yield excessively high values, which, in some cases, even surpass the upper limit of 1. For this reason, these datasets are excluded from the remainder of the analysis.

It should be noted that, for the scaling done based on maxima, the resulting values for s_2 fell in the range of [0.1, 0.19] with a mean of 0.15, which happens to be the center of the s_2 range considered in the study of Quast et al. (2019). This also ensured that resulting SM estimates remain within reasonable ranges and adhere to the plausible upper limit of 0.5, with the maximum SM estimate and the maximum swvl1 measurement for each cell being well-aligned.

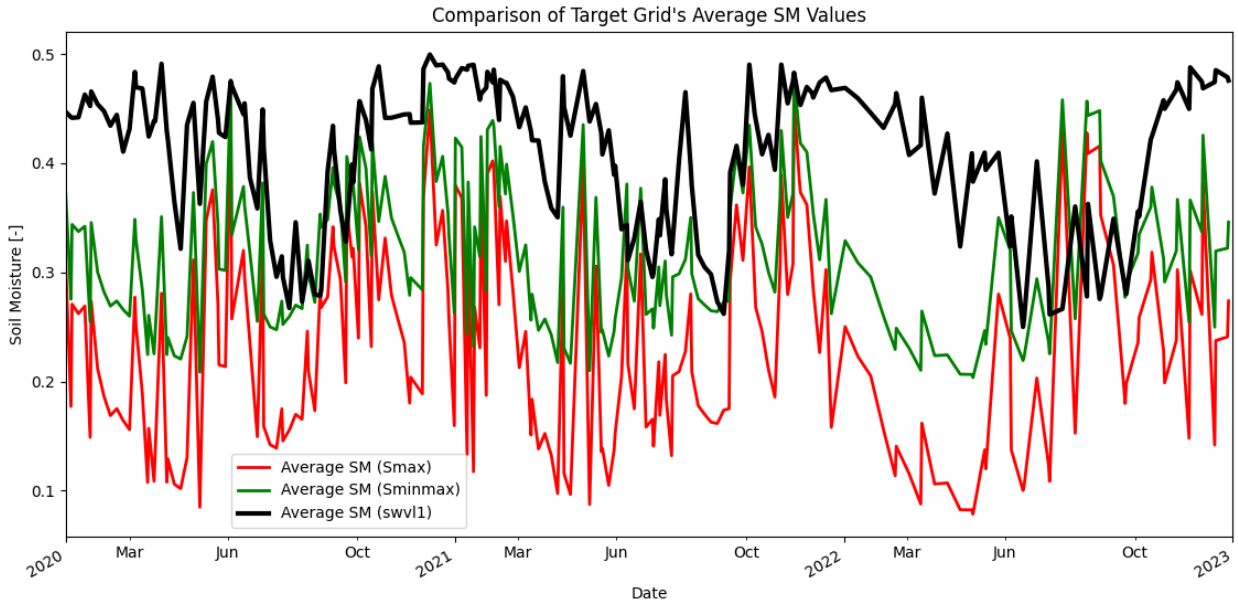

Figure 18 - Timeseries of average SM values for two SM estimate alternatives and baseline SM

Several things can be noted from the figure above, showing SM values averaged over all target grid cells.

First, as expected, the maxima from both scaling alternatives align with the baseline data.

Second, the SM timeseries scaled just based on the maxima seems to reach much lower minima than the baseline data, going below 0.1 in comparison with the baseline values whose floor is around 0.2.

Third, the higher correlation for the period of 2020-2021 can be seen visually as the SM estimates seem to follow more closely the variations in the baseline data on the left side of the figure, with this agreement visibly diminishing on the right side.

Fourth, the SM timeseries obtained using Equation (8), despite being bounded by both the minimum and maximum of the baseline data, still follows an independent trend from the baseline, and consequently doesn't appear to suffer from overfitting. Nonetheless, in order to better understand the downstream effects of each scaling method, both SM datasets, referred to as Smax and Sminmax in the figure and table above, were considered as SM input alternatives for the SM-based inversion approach.

The timeseries plot for the resampled SM data (Figure 24 in Appendix A) is quite similar, with the only difference being that it's slightly smoother due to the resampling. As a result, it doesn't offer any additional insights.

4.1.3. Analysis of SM Estimates using Baseline Irrigation Data

A summary of the results obtained by following the procedure described in Section 3.1.2.7, is presented below.

Table 13 - Summary of weights and areas obtained from irrigation calendars

Cell	Weights								Agricultural Area [km^2]	Total Cell Area [km^2]	Agricultural Area [%]
	Mon	Tue	Wed	Thu	Fri	Sat	Sun	Unknown			
1	0.00	0.04	0.25	0.43	0.00	0.05	0.07	0.16	0.20	0.25	78
2	0.00	0.00	0.00	0.00	0.46	0.31	0.10	0.13	0.17	0.25	69
3	0.01	0.03	0.35	0.39	0.15	0.00	0.00	0.07	0.19	0.25	76
4	0.00	0.00	0.00	0.00	0.06	0.31	0.46	0.16	0.16	0.25	62
5	0.00	0.83	0.00	0.00	0.00	0.00	0.00	0.17	0.03	0.25	11
6	0.61	0.32	0.00	0.00	0.00	0.03	0.00	0.04	0.03	0.25	11

A threshold of 20% was used to filter out any cells that do not have sufficient irrigation calendar data; that is, only cells that have irrigation data for more than 80% of their agricultural fields were considered. Out of these grid cells, Cells 1 and 2 were deemed appropriate for the analysis, as they are mostly covered by agriculture. Moreover, both cells' irrigation schedule falls within two consecutive days of the week. This would make the comparison with SM data, which have an irregular time interval, more feasible.

As a result, plots comparing daily precipitation to each cell's SM estimates (obtained using Equation (8)), the baseline SM data, and their irrigation dates are presented below. The time year considered was the irrigation months (May to September) of 2021. The year of 2021 was chosen due to the presence of a long dry period in this particular year, which allows for the evaluation of the SM estimates' dynamics to irrigation, without the interference from precipitation. The weights for days of week that were less than or equal to 0.1 were disregarded to focus on the influence of the two consecutive days in which each cell was irrigated.

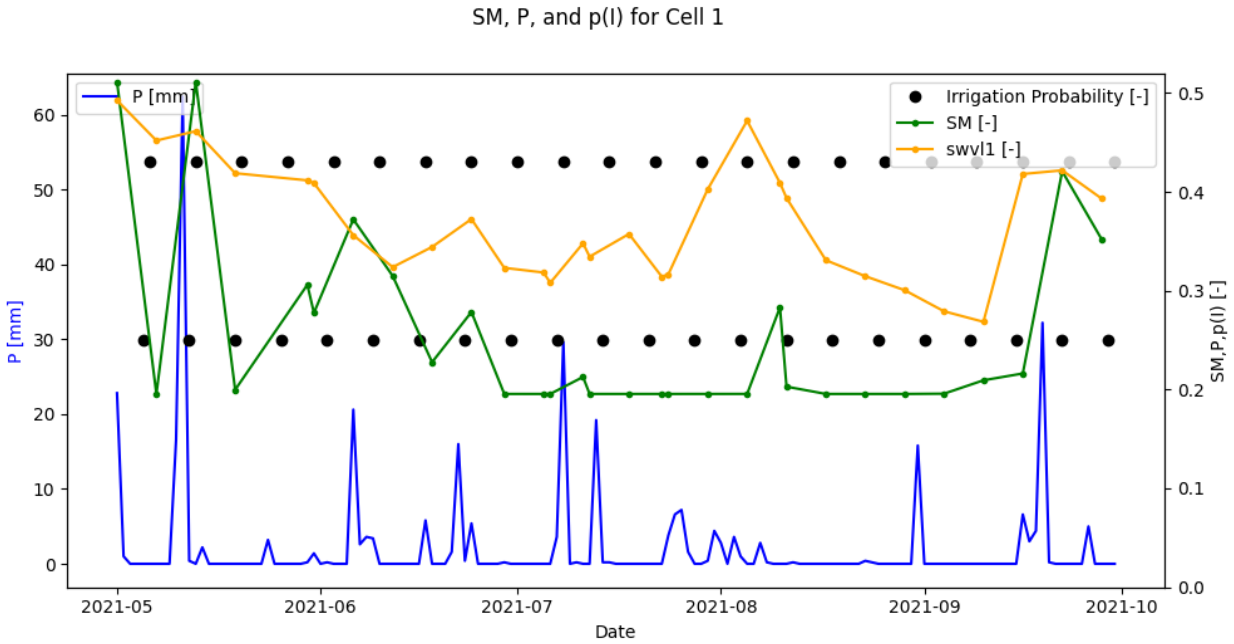

Figure 19 - Plots of SM, P, and p(I) - Cell 1

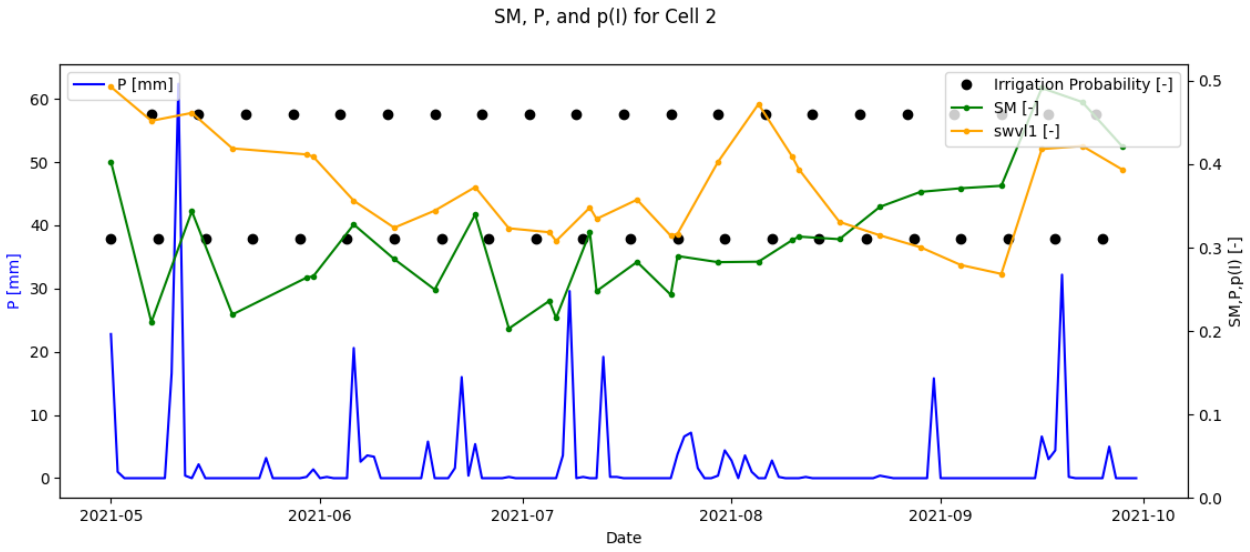

Figure 20 - Plots of SM, P, and p(I) - Cell 2

The figures above allow for several observations. First, the SM dataset appears to be quite reactive with precipitation, with most SM measurements following precipitation events showing an increase compared to the preceding measurement. Second, looking at the dry period in August in Figure 20, we can see increases in SM estimates, despite the lack of precipitation, indicating the occurrence of irrigation. The same is not, reflected, however, in Figure 19.

Regarding the irrigation data, there are several instances where SM is shown to increase, specifically when the measurement happens to directly follow a potential irrigation date, such as in mid-July for cell 2. On the other hand, there are other instances, such as between August and September for Cell 1, where this is not the case.

In general, the correlation between the SM and the irrigation calendars, while being adequate overall, has to be put into context. The intensive selection process allowed the selection of cells that were quite representative, and consequently, limited the effect of having different spatial scales and the effect of having a very mixed and even distribution of irrigation days throughout the areas. However, the reliance on just a few cells of data, in addition to the uncertainty present in the baseline data itself, and its qualitative natures, heavily limit the interpretations that can be made from the analysis.

4.2. SM-Based Inversion

4.2.1. Fitting Results

Detailed statistics for a, b, Z*, and T parameters are found from Table 15 to Table 22 in Appendix A. The first thing to note from the results is the large parameter values for some cells, indicated by the maxima in the relevant tables, which consequently had a great influence on the mean values as well. This justifies the choice to rely on the median values, instead of the mean, to represent the AOI. With that in mind, a summary of the final parameters obtained is presented below.

Table 14 - Fitting results for SM-based inversion algorithm

Fitting Attempt	SM Dataset	a [mm/d]	b [-]	Z* [mm]	T [days]	F [-]
FA1	SM1	40.01	0.84	0	-	0.6
FA2	SM2	82.19	1.81	0		0.6

FA3	SM3	30.22	0.3	986		0.6
FA4	SM4	87.1	1.63	1737		0.6
FA5	SM1	46.72	0.96	0	1.37	0.6
FA6	SM2	96.67	2	0	1.39	0.6
FA7	SM3	31.47	0.29	862	0.01	0.6
FA8	SM4	87.06	1.6	1434	0.01	0.6

For the SM datasets with irregular time intervals (SM1 and SM2), the median value for Z* was always 0. In fact, based on Table 15 and Table 16, even more than 75% of cells got a 0 value for Z* in the attempts without the exponential filter (FA1 and FA2).

This issue of getting a 0 value for Z was avoided with the resampled SM datasets with a regular 12-day time interval (SM3 and SM4), as evident in the Z values obtained for FA3, FA4, FA7, and FA8. This seems to indicate that the switch to a regular time interval led to an improvement in fitting results.

The last two attempts (FA7 and FA8), which consisted of applying the exponential filter to resampled results, however, were not successful. The obtained value of 0.01 was an imposed boundary for the parameter T to avoid a division-by-zero error, since T is placed in the denominator in Equation (28). In fact, based on that equation, a very small value of T would result in a K_n value of 1, which, in turn, would result in SWI=S(t) for Equation (27). In other words, very small values of T mean that the corrected value would be exactly equal to the uncorrected SM value, which would be equivalent to not using the exponential filter. This is validated by the similarity in results between FA3 and FA7, and between FA4 and FA8.

In this context, only the model parameters from FA3 and FA4 were considered to produce irrigation estimates. This is justified by the fact that these two attempts were the only attempts where the values of model parameters obtained were not forced by the imposed lower limits.

It should be noted, however, that the obtained median values of a (30.22 and 87.1 mm/d) are higher than expected (5-40 mm/d) while those of b (0.3 and 1.63) are lower than expected (1-4). The fitted values for these two parameters is still acceptable, nonetheless, as those from FA3 fall within the expected ranges, and those from FA4 are still within the same order of magnitude.

On the other hand, the values obtained for Z*, which represents the soil layer depth in mm, are much higher than the expected ranges for this parameter. Given that the soil moisture estimates were obtained from radar data, they are expected to reflect soil moisture near the surface, and not at large depths. In this context, expected median values for Z*, based on previous studies (Brocca et al., 2014, 2016; Dari et al., 2023)), are expected to range between 10 and 100 mm.

While these deviations can be attributed to many factors, they are expected to be mainly caused by the possible errors in the SM estimations since, as shown in previous studies, it is the most influential variable on the approach's result.

4.2.2. Irrigation Estimates

The irrigation estimates, obtained from fitting attempts FA3, based on resampled SM data that was scaled based on the maxima of N and swvl1, and FA4, , based on resampled SM data that was scaled based on the minima and maxima of N and swvl1, are plotted below, along with the daily and the resampled precipitation timeseries for reference.

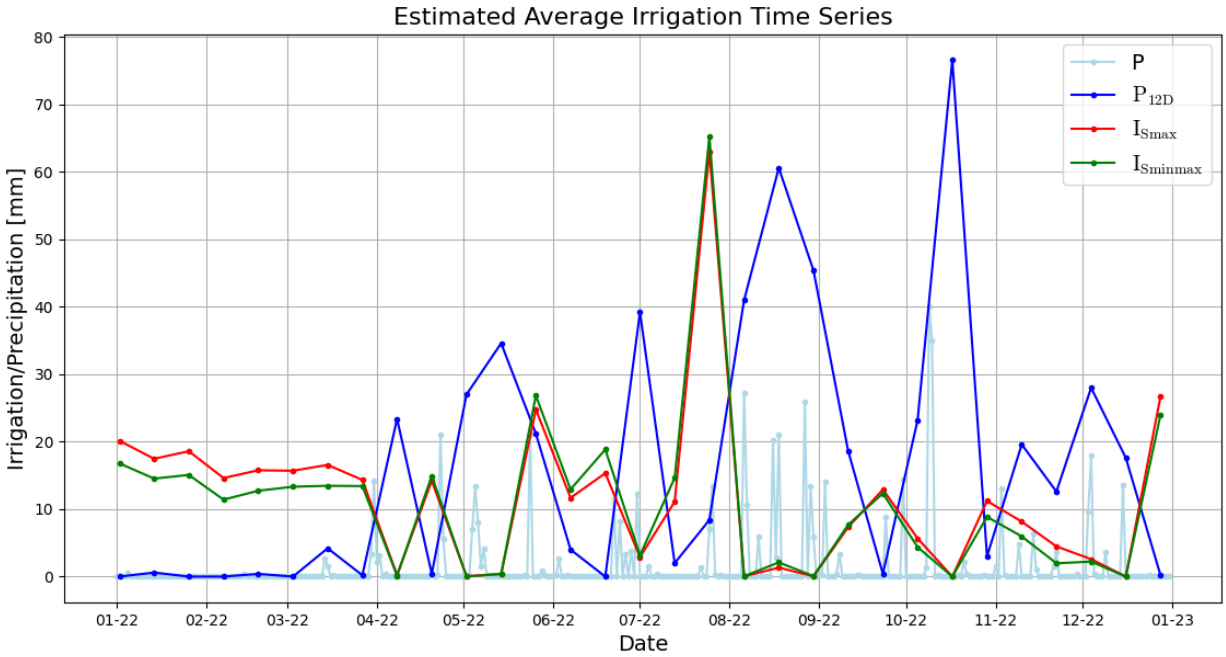

Figure 21 - Timeseries for irrigation and precipitation, averaged across all cells in the target grid

The plot shows little difference in the two irrigation datasets produced. This, however, does not necessarily mean that the method used to scale from the N parameter of the RT1 algorithm to SM values has a relatively low impact on final irrigation results. Considering that both approaches aligned the maxima of the SM estimates to the maxima from the baseline reanalysis SM dataset, the results show that this impact is minimal as long as the SM values are bounded by a reasonable upper limit.

Another observation can be made by comparing the trends from the resampled data to the daily precipitation timeseries. While the temporal resampling may have improved fitting results for the model parameters, it causes the algorithm to fail to capture some of the short-term variations that occur within the adopted time interval. One occurrence of this sort occurs in September, where the resampled data show a huge peak for precipitation, driving irrigation estimates to near-zero values. The daily precipitation data shows, however, that this precipitation peak is indeed the result of strong precipitation events separated by a significant gap (~ 10 days), which, in reality would have warranted irrigation.

4.3. Limitations

Each of the two algorithms considered in this study relies on its own set of assumptions, simplifications, and (empirical or semi-empirical) approximations as its attempts to remain representative of the physical reality while reducing some of the complexity involved to avoid ambiguous fitting. As a result, there's a lot of uncertainty involved, with some of it being inherent to the data used as inputs and another significant part being introduced by the algorithms themselves. This uncertainty is compounded given the fact that the output of one algorithm (RT1) is a largely influential input for the other (SM-based inversion approach). Furthermore, both algorithms are relatively new and still under development, with most of the referenced studies, including this one as well, introducing slight modifications, either for the purpose of exploration or based on a need due to gaps in data availability or quality, and attempting to verify their feasibility.

While this explains the presence of numerous limitations, it is important to shed some light on what the limitations are for two main reasons: first, to put into context the reliability and potential uses of the generated outputs, and, second, to help identify the weaknesses and major areas for improvement which should serve as a starting point for future efforts. This is necessary if we are to unlock their full, promising potential. In this context, the most notable limitations of this study are discussed below.

-Lack of data for baseline irrigation volumes. This has two effects. The first is the inability to do the fitting for the F parameter of the SM-based inversion approach as suggested by Dari et al., 2023. Relying on dry periods preceded by rainy periods, on the assumption that no irrigation is expected to take place directly after a rainy period, adds uncertainty and thus decreases the reliability of obtained results. The second effect is the inability to get quantitative estimates of the error in the produced irrigation dataset due to the lack of reference irrigation data to compare to and the limited analysis possible in the comparison with SM estimates.

-Reliance on reanalysis data with a spatial resolution of 9 km. Given that the study's target spatial resolution is 1km, then the resolution of the reanalysis data considered is 9 times worse. The LAI reanalysis data used in the RT1 fitting is not expected to have a significant impact on fitting results. The swvl1 reanalysis data, on the other hand, is more impactful since it's used for two purposes: to evaluate the accuracy of the RT1 fitting and to scale the N values to SM estimates, which are the main input for the SM2Rain.

-**The use of isotropic phase function to represent the scattering behavior of vegetation.** This was necessary due to the monostatic nature of Sentinel-1 measurements. However, as already mentioned in Section 3.1.1, this leads a possibly poor estimation for the bistatic component of scattering, which is an important aspect of the RT1 approach, compared to previous approaches that neglected the first-order contributions.

-The inability to apply the exponential filter for SM estimates. While the filter is expected to reduce the noise in the SM signal, which could potentially improve the fitting obtained from the RT1 approach, the inclusion of an additional parameter, T, to be fitted where the Sentinel-1 data already has the possibility of leading to underdetermined fitting results prevented its use.

-Precipitation and temperature data were obtained from one meteo-station. While temperature has a relatively high spatial correlation, at least in the case of the study areas considered where there isn't a large difference in elevation, the same cannot be said about precipitation. While the station is more or less centered around the study area, considering that one station's measurement of precipitation is representative of an area of 73 km^2 is a limitation. Furthermore, the fact that temperature data is used to calculate PET means that both PET and P, which constitute two of the three main inputs for the SM-based inversion approach, are assumed to be equal for the whole study area.

-**Reliance on the simplified Hargreaves formula to calculate PET**. Had the FAO approach been considered to get ET from PET, this would not be expected to have a major impact on results (as shown by Dari et al., 2022). The study, however, relied on the more recent approach of relying on the parameter F as a correction factor to derive ET from PET, meaning that this simplification could have a slightly higher impact.

5. CONCLUSIONS

The study provided a thorough overview on the current state of water management through the use of satellite data.

It highlighted the major limitations of radar data, starting with the most important one, data availability. Two main conclusions can be made from the research done into the alternative radar missions. The first is the issue of data accessibility. This is emphasized by the fact that, after months of communication with the relevant authorities, only four out of the eight alternative radar missions were accessed for browsing. The study quantitatively showcased the importance of having alternatives by measuring, through the Pearson correlation coefficient, how the quality of soil moisture estimates obtained from RT1 deteriorated after the loss of Sentinel-1B. The second conclusion derived from that research is the great potential of radar data. This is demonstrated by the number of alternatives identified, the fact the many of them are recent, with half of the alternatives being launched after 2016, and the plans made to launch more SARs in the future. This, together with the continuous improvement in the spatial and temporal resolutions offered by the new satellites, and the increasing algorithms being developed to make use of this data is definitely a reason for optimism.

The study, then, proceeded to apply two prominent algorithms that make use of radar data over 73 km^2 of agricultural areas in Caluso, Piemonte. The first algorithm, RT1, allowed the retrieval of soil moisture estimates at a resolution of ~ 1 km. The major limitations faced were the reliance on reanalysis data and the simplified representation of vegetation scattering through the isotropic phase function. The first disadvantage of using reanalysis data is its relatively lower spatial scale of 9 km, which adds uncertainty to the modeled results. The second disadvantage is for the LAI data, which doesn't have any inter-annual variability because, unlike other reanalysis parameters, it is modeled via a more simplistic approach. This is not expected to have a significant impact on results, however, due to its limited use as a proxy for the optical depth parameter, which isn't very influential on the result outputs. Regarding the isotropic function, this is, until now, a necessary simplification due to the monostatic nature of Sentinel-1 observations, in order to avoid ambiguous parameter results.

The second algorithm, the SM-based inversion approach, provided one example of the utility of soil moisture data, as it adopted the data obtained from RT1 to produce irrigation estimates. The first limitation faced in this approach was the inability to use the exponential filter, as demonstrated by the unsuccessful fitting attempts that were made while trying to consider it. Its use in further studies, in case auxiliary data allowed for the determination of the T parameter would provide a valuable removal of noise from the SM estimates. Another limitation, despite its expectedly low impact, as demonstrated in previous studies, was the reliance on the simplified Hargreaves formula due to lack of additional data needed for the more thorough PM equation. The third limitation was the adoption of the same P and E timeseries for all cells in the area of interest. This also allows for room for improvement if better alternatives for this data are made available. The last limitation to note is the lack of baseline irrigation volumes. This prevents the most influential limitation of this study. In addition to the limited interpretations obtained from the analysis with irrigation calendars, this prevented the quantitative analysis of the performance of the SM-based inversion algorithm by direct comparison to baseline volumes. Moreover, it necessitated the reliance on an alternative method to fit the F parameter, adding further uncertainty to the algorithm's outputs. This highlights the importance of having better availability and sharing of irrigation volume data. The availability of such data in the future would open up a huge range of possibilities to improve upon the results obtained in this study. Moreover, it would help

accelerate the development of algorithms, such as this one, and thus bring us closer to a better state of water monitoring and management.

Despite the limitations presented above, this study showed the great potential of these algorithms. It also showed, despite the fact that they're still quite recent and still heavily under development, with lots of room for improvement, that they can play a major role in better in water management, which is a much needed first step towards better handling of this invaluable resource, to increase our resilience to the ever-growing issue of climate change.

APPENDIX A

RT1

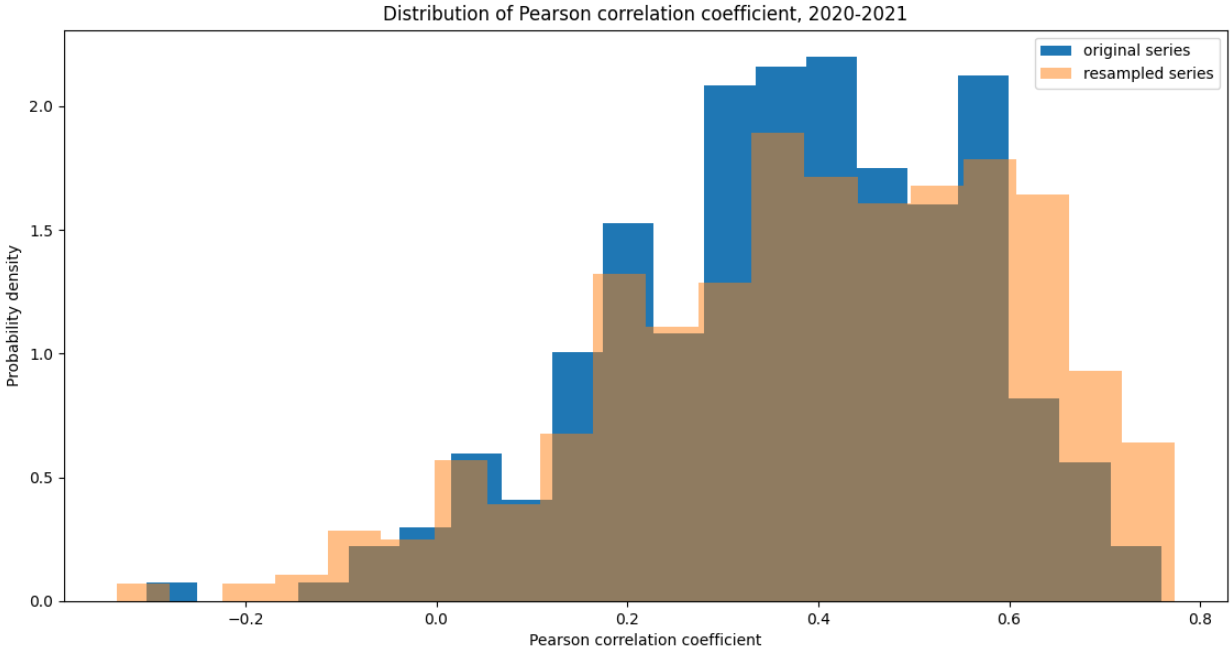

Figure 22 - Comparison of Pearson correlation density plots for RT1 results before and after resampling – 2020-2021

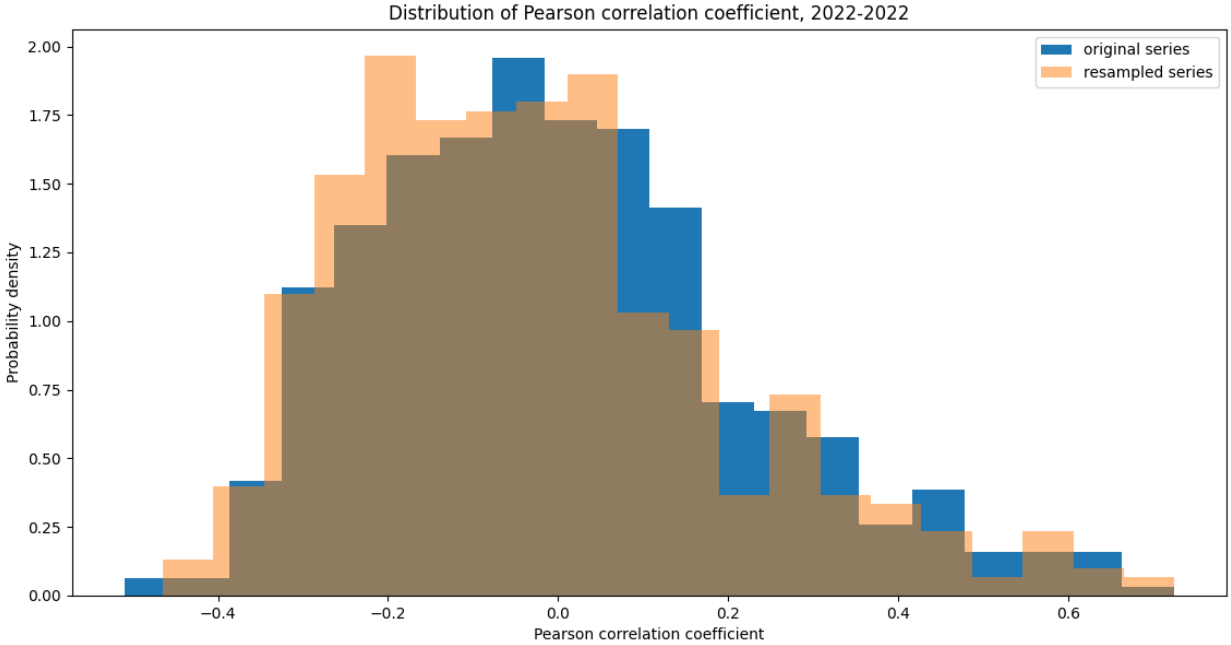

Figure 23 - Comparison of Pearson correlation density plots for RT1 results before and after resampling – 2022

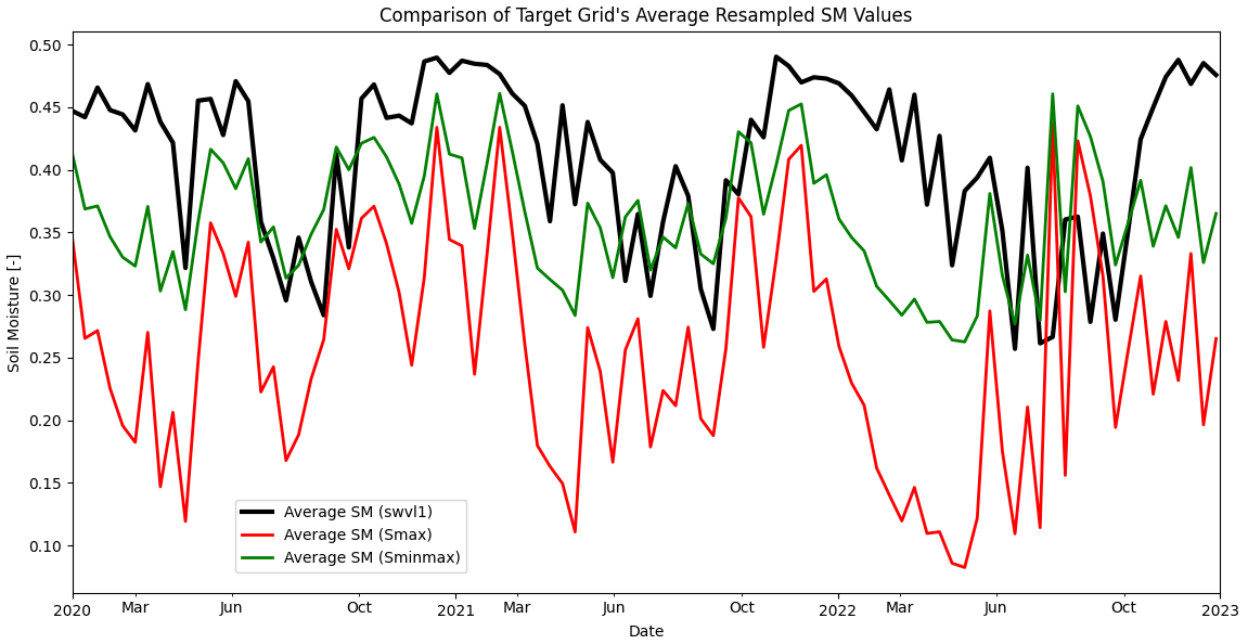

Figure 24 - Timeseries of average resampled SM values for two SM estimate alternatives and baseline SM

SM-Based Inversion Approach

Table 15 - Statistics for a, b, and Z - fitting attempt 1*

Fitting Attempt 1			
Metric	**a [mm/d]**	**b [-]**	**Z* [mm]**
count	505	505	505
mean	242.89	1.06	2.99
std	2248.45	1.05	9.00
min	12.09	0.00	0.00
25%	28.33	0.54	0.00
50%	40.01	0.84	0.00
75%	65.73	1.27	0.00
max	45430.23	10.30	80.68

Table 16 - Statistics for a, b, and Z - fitting attempt 2*

Fitting Attempt 2			
Metric	**a [mm/d]**	**b [-]**	**Z* [mm]**
count	505	505	505
mean	1279.86	2.09	4.03
std	12783.13	1.53	12.27
min	11.51	0.00	0.00
25%	47.87	1.28	0.00
50%	82.19	1.81	0.00
75%	161.06	2.49	0.00
max	256187.17	13.28	115.30

Table 17 - Statistics for a, b, and Z - fitting attempt 3*

Fitting Attempt 3			
Metric	**a [mm/d]**	**b [-]**	**Z* [mm]**
count	505	505	505
mean	44.62	0.45	934.06
std	50.86	0.52	459.25
min	16.31	0.00	0.00
25%	21.16	0.06	652.46
50%	30.22	0.30	986.99
75%	41.90	0.58	1218.14
max	394.49	3.03	2467.67

Table 18 - Statistics for a, b, and Z - fitting attempt 4*

Fitting Attempt 4			
Metric	**a [mm/d]**	**b [-]**	**Z* [mm]**
count	505	505	505
mean	6919.01	2.18	1694.19
std	37277.99	2.29	844.58
min	14.92	0.00	0.00
25%	40.31	0.84	1214.70
50%	87.10	1.63	1737.10
75%	198.65	2.67	2220.80
max	354060.70	11.98	4271.19

Table 19 - Statistics for a, b, Z, and T - fitting attempt 5*

Fitting Attempt 5				
Metric	**a [mm/d]**	**b [-]**	**Z* [mm]**	**T [days]**
count	505	505	505	505
mean	1417.47	1.21	16.86	37.95
std	21757.40	1.20	54.50	775.76
min	12.18	0.00	0.00	0.01
25%	30.54	0.60	0.00	1.25
50%	46.72	0.96	0.00	1.37
75%	84.26	1.47	16.60	1.56
max	445626.77	13.09	639.23	17425.84

Table 20 - Statistics for a, b, Z, and T - fitting attempt 6*

Fitting Attempt 6				
Metric	**a [mm/d]**	**b [-]**	**Z* [mm]**	**T [days]**
count	505	505	505	505
mean	1271.45	2.32	19.14	14.92
std	8318.94	1.63	54.80	292.66
min	11.37	0.00	0.00	0.01
25%	57.06	1.41	0.00	1.04
50%	96.67	2.00	0.00	1.39
75%	239.87	2.90	22.43	1.58
max	125173.91	11.94	750.04	6577.19

Table 21 - Statistics for a, b, Z, and T - fitting attempt 7*

Fitting Attempt 7				
Metric	**a [mm/d]**	**b [-]**	**Z* [mm]**	**T [days]**
count	505	505	505	505
mean	48.16	0.43	907.52	87.98
std	77.62	0.53	982.11	1040.70
min	18.18	0.00	0.00	0.01
25%	21.72	0.04	582.22	0.01
50%	31.47	0.29	862.44	0.01
75%	43.27	0.57	1097.57	0.01
max	1309.48	3.42	19190.03	20036.91

Table 22 - Statistics for a, b, Z, and T - fitting attempt 8*

Fitting Attempt 8				
Metric	**a [mm/d]**	**b [-]**	**Z* [mm]**	**T [days]**
count	505	505	505	505
mean	3707.65	2.07	1383.05	20.29
std	27698.93	2.07	776.38	272.30
min	16.39	0.00	0.00	0.01
25%	42.70	0.83	897.75	0.01
50%	87.06	1.60	1434.38	0.01
75%	202.65	2.55	1869.66	0.01
max	433502.27	12.43	4673.37	4643.56

REFERENCES

Abolafia-Rosenzweig, R., Livneh, B., Small, E. E., & Kumar, S. V. (2019). Soil Moisture Data Assimilation to Estimate Irrigation Water Use. In Journal of Advances in Modeling Earth Systems (Vol. 11, Issue 11, pp. 3670–3690). American Geophysical Union (AGU). https://doi.org/10.1029/2019ms001797

Alan D. Snow, Jeff Whitaker, Micah Cochran, Idan Miara, Joris Van den Bossche, Chris Mayo, Paul Cochrane, Greg Lucas, Jos de Kloe, Charles Karney, Filipe, Bas Couwenberg, Guillaume Lostis, Justin Dearing, George Ouzounoudis, Brendan Jurd, Christoph Gohlke, Daniel McDonald, David Hoese, … DWesl. (2023). pyproj4/pyproj: 3.6.1 Release (3.6.1). *Zenodo*. https://doi.org/10.5281/zenodo.8365173

Alan D. Snow, Martin Raspaud, David Brochart, Kirill Kouzoubov, Scott Henderson, Rémi Braun, Alessandro Amici, stefank0, Taher Chegini, RichardScottOZ, Ray Bell, Mike Taves, Mauricio Cordeiro, sangzi-liang, Seth Caldwell, Seth Miller, The Gitter Badger, Tom Augspurger, Yvonne Fröhlich, … Fred Bunt. (2024). corteva/rioxarray: 0.15.1 Release (0.15.1). *Zenodo*. https://doi.org/10.5281/zenodo.10557113

Alexandridis, T. K., Panagopoulos, A., Galanis, G., Alexiou, I., Cherif, I., Chemin, Y., Stavrinos, E., Bilas, G., & Zalidis, G. C. (2013). Combining remotely sensed surface energy fluxes and GIS analysis of groundwater parameters for irrigation system assessment. In Irrigation Science (Vol. 32, Issue 2, pp. 127–140). Springer Science and Business Media LLC. https://doi.org/10.1007/s00271-013-0419-8

Allen, R. G., Pereira, L. S., Raes, D., & Smith, M. (1998). Crop evapotranspiration-Guidelines for computing crop water requirements-FAO Irrigation and drainage paper 56. *Fao, Rome*, *300*(9), D05109

Álvarez-Perez, J. L. (2001). An extension of the IEM/IEMM surface scattering model. *Waves in Random Media, 11*(3), 307–329. https://doi.org/10.1088/0959-7174/11/3/308

Álvarez-Pérez, J. L. (2012). The IEM2M rough-surface scattering model for complex-permittivity scattering media. *Waves in Random and Complex Media, 22*(2), 207–233. https://doi.org/10.1080/17455030.2011.649147

Attema, E., & Ulaby, F. T. (1978). Vegetation modeled as a water cloud. *Radio Science, 13*(2), 357–364. https://doi.org/10.1029/rs013i002p00357

Balenzano, A., Satalino, G., Pauwels, V., & Mattia, F. (2011). Soil moisture retrieval from dense temporal series of C-band SAR data over agricultural sites. In 2011 IEEE International Geoscience and Remote Sensing Symposium. IGARSS 2011 - 2011 IEEE International Geoscience and Remote Sensing Symposium. IEEE. https://doi.org/10.1109/igarss.2011.6049883

Bauer-Marschallinger, B., Freeman, V., Cao, S., Paulik, C., Schaufler, S., Stachl, T., Modanesi, S., Massari, C., Ciabatta, L., Brocca, L., & Wagner, W. (2019). Toward global soil moisture monitoring with Sentinel-1: Harnessing assets and overcoming obstacles. *IEEE Transactions on Geoscience and Remote Sensing, 57*(1), 520–539. https://doi.org/10.1109/tgrs.2018.2858004

Boori, M. S., Choudhary, K., Paringer, R., & Kupriyanov, A. (2021). Eco-environmental quality assessment based on pressure-state-response framework by remote sensing and GIS. In Remote Sensing Applications: Society and Environment (Vol. 23, p. 100530). Elsevier BV. https://doi.org/10.1016/j.rsase.2021.100530

Brocca, L., Ciabatta, L., Massari, C., Camici, S., & Tarpanelli, A. (2017). Soil moisture for hydrological applications: open questions and new opportunities. *Water*, 9(2), 140. https://doi.org/10.3390/w9020140

Brocca, L., Ciabatta, L., Massari, C., Moramarco, T., Hahn, S., Hasenauer, S., Kidd, R., Dorigo, W., Wagner, W., & Levizzani, V. (2014). Soil as a natural rain gauge: Estimating global rainfall from satellite soil moisture data. Journal of Geophysical Research: Atmospheres, 119(9), 5128–5141. https://doi.org/10.1002/2014jd021489

Brocca, L., Massari, C., Ciabatta, L., Moramarco, T., Penna, D., Zuecco, G., Pianezzola, L., Borga, M., Matgen, P., & Martínez-Fernández, J. (2015). Rainfall estimation from in situ soil moisture observations at several sites in Europe: an evaluation of the SM2RAIN algorithm. *Journal of Hydrology and Hydromechanics*, 63(3), 201–209. https://doi.org/10.1515/johh-2015-0016

Brocca, L., Pellarin, T., Crow, W. T., Ciabatta, L., Massari, C., Ryu, D., Su, C., Rüdiger, C., & Kerr, Y. H. (2016). Rainfall estimation by inverting SMOS soil moisture estimates: A comparison of different methods over Australia. *Journal of Geophysical Research: Atmospheres*, 121(20), 12,062-12,079. https://doi.org/10.1002/2016jd025382

Caswell, T.A., de Andrade, E.S., Lee, A., Droettboom, M., Hoffmann, T., Klymak, J., Hunter, J., Firing, E., Stansby, D., Varoquaux, N., Nielsen, J.H., Gustafsson, O., Sunden, K., Root, B., May, R., Hannah, Elson, P., Seppänen, J.K., Lee, J, …, Silvester, S. (2024). matplotlib/matplotlib: REL: v3.7.5 (v3.7.5). *Zenodo*. https://doi.org/10.5281/zenodo.10669804

Chandrasekhar, S. (1960). Radiative transfer. *Courier Corporation.*

Chen, K., Chen, K., Li, Z., & Liu, Y. (2015). Extension and validation of an advanced integral equation model for bistatic scattering from rough surfaces. *Electromagnetic Waves, 152*, 59–76. https://doi.org/10.2528/pier15011409

Copernicus Climate Change Service (2024). *ERA5-Land hourly data from 1950 to present*. Copernicus Climate Change Service (C3S) Climate Data Store (CDS). https://doi.org/10.24381/cds.e2161bac (Accessed on 26-01-2024)

Dari, J., Brocca, L., Modanesi, S., Massari, C., Tarpanelli, A., Barbetta, S., Quast, R., Vreugdenhil, M., Freeman, V., Barella-Ortiz, A., Quintana-Seguí, P., Bretreger, D., & Volden, E. (2023). Regional data sets of high-resolution (1 and 6 km) irrigation estimates from space. In Earth System Science Data (Vol. 15, Issue 4, pp. 1555–1575). Copernicus GmbH. https://doi.org/10.5194/essd-15-1555-2023

Dari, J., Brocca, L., Quintana-Seguí, P., Escorihuela, M. J., Stefan, V., & Morbidelli, R. (2020). Exploiting High-Resolution Remote Sensing Soil Moisture to Estimate Irrigation Water Amounts over a Mediterranean Region. In Remote Sensing (Vol. 12, Issue 16, p. 2593). MDPI AG. https://doi.org/10.3390/rs12162593

Dari, J., Quintana-Seguí, P., Morbidelli, R., Saltalippi, C., Flammini, A., Giugliarelli, E., Escorihuela, M. J., Stefan, V., & Brocca, L. (2022). Irrigation estimates from space: Implementation of different approaches to model the evapotranspiration contribution within a soil-moisture-based inversion algorithm. In Agricultural Water Management (Vol. 265, p. 107537). Elsevier BV. https://doi.org/10.1016/j.agwat.2022.107537

De Lannoy, G. J. M., & Reichle, R. H. (2016a). Global Assimilation of Multiangle and Multipolarization SMOS Brightness Temperature Observations into the GEOS-5 Catchment Land Surface Model for Soil

Moisture Estimation. In Journal of Hydrometeorology (Vol. 17, Issue 2, pp. 669–691). American Meteorological Society. https://doi.org/10.1175/jhm-d-15-0037.1

De Lannoy, G. J. M., & Reichle, R. H. (2016b). Assimilation of SMOS brightness temperatures or soil moisture retrievals into a land surface model. In Hydrology and Earth System Sciences (Vol. 20, Issue 12, pp. 4895–4911). Copernicus GmbH. https://doi.org/10.5194/hess-20-4895-2016

Doorenbos, J., & Pruitt, W. O. (1977). Background and development of methods to predict reference crop evapotranspiration (ETo). *Appendix II in FAO-ID-24*, 108-119

Dorigo, W., Dietrich, S., Aires, F., Brocca, L., Carter, S., Cretaux, J.-F., Dunkerley, D., Enomoto, H., Forsberg, R., Güntner, A., Hegglin, M. I., Hollmann, R., Hurst, D. F., Johannessen, J. A., Kummerow, C., Lee, T., Luojus, K., Looser, U., Miralles, D. G., … Aich, V. (2021). Closing the Water Cycle from Observations across Scales: Where Do We Stand? In Bulletin of the American Meteorological Society (Vol. 102, Issue 10, pp. E1897–E1935). American Meteorological Society. https://doi.org/10.1175/bams-d-19-0316.1

Duffie, J. A., & Beckman, W. (2013). Solar engineering of thermal processes. *Hoboken*. https://doi.org/10.1002/9781118671603

European Environment Agency. (2023, Aug 29). Water use in Europe – Quantity and quality face big challenges.

European Space Agency. (2022). Sentinel-1B in-flight anomaly summary report. *ESA*. https://sentinel.esa.int/documents/247904/4819394/Sentinel-1B+In-Flight+Anomaly+Summary+Report.pdf

European Space Agency. (2023). Loss of flight VV22: Independent Enquiry Commission announces conclusions. *ESA*. https://www.esa.int/Newsroom/Press_Releases/Loss_of_flight_VV22_Independent_Enquiry_Commission_announces_conclusions

Famiglietti, J. S., & Wood, E. F. (1994). Multiscale modeling of spatially variable water and energy balance processes. *Water Resources Research, 30*(11), 3061–3078. https://doi.org/10.1029/94wr01498

Filipponi, F. (2019). Sentinel-1 GRD Preprocessing Workflow. *Proceedings, 18*, 6201. https://doi.org/10.3390/ecrs-3-06201

Foley, J. A., Ramankutty, N., Brauman, K. A., Cassidy, E. S., Gerber, J. S., Johnston, M., Mueller, N. D., O'Connell, C., Ray, D. K., West, P. C., Balzer, C., Bennett, E. M., Carpenter, S. R., Hill, J., Monfreda, C., Polasky, S., Rockström, J., Sheehan, J., Siebert, S., … Zaks, D. P. M. (2011). Solutions for a cultivated planet. In Nature (Vol. 478, Issue 7369, pp. 337–342). Springer Science and Business Media LLC. https://doi.org/10.1038/nature10452

Foust, J. (2023). Arianespace wins Vega contract for Italian imaging satellite constellation. *SpaceNews*. https://spacenews.com/arianespace-wins-vega-contract-for-italian-imaging-satellite-constellation/

Gupta, H. V., Kling, H., Yılmaz, K. K., & Martínez, G. (2009). Decomposition of the mean squared error and NSE performance criteria: Implications for improving hydrological modelling. *Journal of Hydrology, 377*(1–2), 80–91. https://doi.org/10.1016/j.jhydrol.2009.08.003

Haiyan, D., & Hai-Mei, W. (2021). Influence of rainfall events on soil moisture in a typical steppe of Xilingol. *Physics and Chemistry of the Earth, Parts a/B/C, 121*, 102964. https://doi.org/10.1016/j.pce.2020.102964

Hargreaves, G. H., & Samani, Z. (1982). Estimating potential evapotranspiration. *Journal of the Irrigation and Drainage Division, 108*(3), 225–230. https://doi.org/10.1061/jrcea4.0001390

Hargreaves, G. H., & Samani, Z. (1985). Reference Crop Evapotranspiration from Temperature. *Applied Engineering in Agriculture, 1*(2), 96–99. https://doi.org/10.13031/2013.26773

Harris, C.R., Millman, K.J., van der Walt, S.J. et al. Array programming with NumPy. *Nature 585*, 357–362 (2020). https://doi.org/10.1038/s41586-020-2649-2

Hoyer, S., Roos, M., Joseph, H., Magin, J., Cherian, D., Fitzgerald, C., Hauser, M., Fujii, K., Maussion, F., Imperiale, G., Clark, S., Kleeman, A., Nicholas, T., Kluyver, T., Westling, J., Munroe, J., Amici, A., Barghini, A., Banihirwe, A., … Wolfram, P. J. (2024). xarray (v2024.02.0). *Zenodo*. https://doi.org/10.5281/zenodo.10676856

https://www.eea.europa.eu/signals-archived/signals-2018-content-list/articles/water-use-in-europe-2014

Jalilvand, E., Abolafia-Rosenzweig, R., Tajrishy, M., & Das, N. (2021). Evaluation of SMAP/Sentinel 1 High-Resolution Soil Moisture Data to Detect Irrigation Over Agricultural Domain. In IEEE Journal of Selected Topics in Applied Earth Observations and Remote Sensing (Vol. 14, pp. 10733–10747). Institute of Electrical and Electronics Engineers (IEEE). https://doi.org/10.1109/jstars.2021.3119228

Jalilvand, E., Tajrishy, M., Hashemi, S. a. G. Z., & Brocca, L. (2019). Quantification of irrigation water using remote sensing of soil moisture in a semi-arid region. *Remote Sensing of Environment, 231*, 111226. https://doi.org/10.1016/j.rse.2019.111226

Knüppe, K., & Meissner, R. (2016). Drivers and barriers towards sustainable water and land management in the Olifants-Doorn Water Management Area, South Africa. In Environmental Development (Vol. 20, pp. 3–14). Elsevier BV. https://doi.org/10.1016/j.envdev.2016.09.002

Lawford, R., Strauch, A., Toll, D., Fekete, B., & Cripe, D. (2013). Earth observations for global water security. In Current Opinion in Environmental Sustainability (Vol. 5, Issue 6, pp. 633–643). Elsevier BV. https://doi.org/10.1016/j.cosust.2013.11.009

Lawley, V., Lewis, M., Clarke, K., & Ostendorf, B. (2016). Site-based and remote sensing methods for monitoring indicators of vegetation condition: An Australian review. In Ecological Indicators (Vol. 60, pp. 1273–1283). Elsevier BV. https://doi.org/10.1016/j.ecolind.2015.03.021

Lawston, P. M., Santanello, J. A., Jr, & Kumar, S. V. (2017). Irrigation Signals Detected From SMAP Soil Moisture Retrievals. In Geophysical Research Letters (Vol. 44, Issue 23). American Geophysical Union (AGU). https://doi.org/10.1002/2017gl075733

Lawston, P. M., Santanello, J. A., Jr., Zaitchik, B. F., & Rodell, M. (2015). Impact of Irrigation Methods on Land Surface Model Spinup and Initialization of WRF Forecasts. In Journal of Hydrometeorology (Vol. 16, Issue 3, pp. 1135–1154). American Meteorological Society. https://doi.org/10.1175/jhm-d-14-0203.1

Lechner, A. M., Foody, G. M., & Boyd, D. S. (2020). Applications in Remote Sensing to Forest Ecology and Management. In One Earth (Vol. 2, Issue 5, pp. 405–412). Elsevier BV. https://doi.org/10.1016/j.oneear.2020.05.001

Lievens, H., Martens, B., Verhoest, N. E. C., Hahn, S., Reichle, R. H., & Miralles, D. G. (2017a). Assimilation of global radar backscatter and radiometer brightness temperature observations to improve soil moisture and land evaporation estimates. In Remote Sensing of Environment (Vol. 189, pp. 194–210). Elsevier BV. https://doi.org/10.1016/j.rse.2016.11.022

Lievens, H., Reichle, R. H., Liu, Q., De Lannoy, G. J. M., Dunbar, R. S., Kim, S. B., Das, N. N., Cosh, M., Walker, J. P., & Wagner, W. (2017b). Joint Sentinel-1 and SMAP data assimilation to improve soil moisture estimates. In Geophysical Research Letters (Vol. 44, Issue 12, pp. 6145–6153). American Geophysical Union (AGU). https://doi.org/10.1002/2017gl073904

Machairas, I. (2022, September 13). How to estimate Potential Hargreaves Evaporation on Python (easy and quick explanation) — Hydrology. Medium. https://medium.com/@ilmachairas/how-to-estimate-hargreaves-evaporation-on-python-easy-and-quick-explanation-hydrology-f920518bd3e3 (Accessed on 26-02-2024)

Merlin, O., Escorihuela, M. J., Mayoral, M. A., Hagolle, O., Bitar, A. A., & Kerr, Y. H. (2013). Self-calibrated evaporation-based disaggregation of SMOS soil moisture: An evaluation study at 3 km and 100 m resolution in Catalunya, Spain. *Remote Sensing of Environment, 130*, 25–38. https://doi.org/10.1016/j.rse.2012.11.008

Modanesi, S., Dari, J., Massari, C., Tarpanelli, A., Barbetta, S., De Lannoy, G., Gruber, A., Lievens, H., Bechtold, M., Quast, R., Vreugdenhil, M., Zribi, M., Page, M. L., & Brocca, L. (2021). A comparison between satellite- and model-based approaches developed in the ESA Irrigation+project framework to estimate irrigation quantities. *IEEE International Workshop on Metrology for Agriculture and Forestry (MetroAgriFor)*, 268-272, https://doi.org/10.1109/metroagrifor52389.2021.9628453

Modanesi, S., Massari, C., Bechtold, M., Lievens, H., Tarpanelli, A., Brocca, L., Zappa, L., & De Lannoy, G. J. M. (2022). Challenges and benefits of quantifying irrigation through the assimilation of Sentinel-1 backscatter observations into Noah-MP. In Hydrology and Earth System Sciences (Vol. 26, Issue 18, pp. 4685–4706). Copernicus GmbH. https://doi.org/10.5194/hess-26-4685-2022

Muñoz Sabater, J. (2019). *ERA5-Land hourly data from 1950 to present*. Copernicus Climate Change Service (C3S) Climate Data Store (CDS). https://doi.org/10.24381/cds.e2161bac (Accessed on 26-01-2024)

Mutiga, J. K., Mavengano, S. T., Zhongbo, S., Woldai, T., & Becht, R. (2010). Water Allocation as a Planning Tool to Minimise Water Use Conflicts in the Upper Ewaso Ng'iro North Basin, Kenya. In Water Resources Management (Vol. 24, Issue 14, pp. 3939–3959). Springer Science and Business Media LLC. https://doi.org/10.1007/s11269-010-9641-9

Nian, Y., Li, X., Zhou, J., & Hu, X. (2013). Impact of land use change on water resource allocation in the middle reaches of the Heihe River Basin in northwestern China. In Journal of Arid Land (Vol. 6, Issue 3, pp. 273–286). Springer Science and Business Media LLC. https://doi.org/10.1007/s40333-013-0209-4

Nie, W., Zaitchik, B. F., Rodell, M., Kumar, S. V., Anderson, M. C., & Hain, C. (2018). Groundwater Withdrawals Under Drought: Reconciling GRACE and Land Surface Models in the United States High

Plains Aquifer. In Water Resources Research (Vol. 54, Issue 8, pp. 5282–5299). American Geophysical Union (AGU). https://doi.org/10.1029/2017wr022178

Ozdogan, M., Rodell, M., Beaudoing, H. K., & Toll, D. L. (2010). Simulating the Effects of Irrigation over the United States in a Land Surface Model Based on Satellite-Derived Agricultural Data. In Journal of Hydrometeorology (Vol. 11, Issue 1, pp. 171–184). American Meteorological Society. https://doi.org/10.1175/2009jhm1116.1

Quast, R. (2023). TUW-GEO/rt1: RT1 v2.0 (v2.0). *Zenodo*. https://doi.org/10.5281/zenodo.8363614

Quast, R., & Wagner, W. (2016). Analytical solution for first-order scattering in bistatic radiative transfer interaction problems of layered media. *Applied Optics, 55*(20), 5379. https://doi.org/10.1364/ao.55.005379

Quast, R., Albergel, C., Calvet, J., & Wagner, W. (2019). A Generic First-Order Radiative Transfer Modelling Approach for the Inversion of Soil and Vegetation Parameters from Scatterometer Observations. *Remote Sensing, 11*(3), 285. https://doi.org/10.3390/rs11030285

Quast, R., Wagner, W., Bauer-Marschallinger, B., & Vreugdenhil, M. (2023). Soil moisture retrieval from Sentinel-1 using a first-order radiative transfer model—A case-study over the Po-Valley. *Remote Sensing of Environment*, 295, 113651. https://doi.org/10.1016/j.rse.2023.113651

Rocklin, M. (2015). Dask: Parallel Computation with Blocked algorithms and Task Scheduling. *Proceedings of the Python in Science Conferences*. https://doi.org/10.25080/majora-7b98e3ed-013

Singh, A., Meena, G., Kumar, S., & Gaurav, K. (2018). ANALYSIS OF THE EFFECT OF INCIDENCE ANGLE AND MOISTURE CONTENT ON THE PENETRATION DEPTH OF L- AND S-BAND SAR SIGNALS INTO THE GROUND SURFACE. *ISPRS Annals of the Photogrammetry, Remote Sensing and Spatial Information Sciences*. https://doi.org/10.5194/ISPRS-ANNALS-IV-5-197-2018

Stroud, P. D. (1999). A recursive exponential filter for time-sensitive data. *Los Alamos National Laboratory, Tech. Rep. LAUR-99-5573*, 131.

The pandas development team. (2024). pandas-dev/pandas: Pandas (v2.2.0). *Zenodo*. https://doi.org/10.5281/zenodo.10537285

Torres, R., Snoeij, P., Geudtner, D., Bibby, D., Davidson, M., Attema, E., Potin, P., Rommen, B., Floury, N., Brown, M., Traver, I. N., Deghaye, P., Duesmann, B., Rosich, B., Miranda, N., Bruno, C., L'Abbate, M., Croci, R., Pietropaolo, A., . . . Rostan, F. (2012). GMES Sentinel-1 mission. *Remote Sensing of Environment, 120*, 9–24. https://doi.org/10.1016/j.rse.2011.05.028

UNESCO. (2021). The United Nations World Water Development Report 2021: Valuing Water. United Nations.

Van den Bossche, J., Jordahl, K., Fleischmann, M., McBride, J., Richards, M., Wasserman, J., Badaracco, A.G., Snow, A.D., Ward, B., Gerard, J., Tratner, J., Perry, M., Farmer, C., Hjelle, G.A., Taves, M., Hoeven, E., Cochran, M., Rraymondgh, Bartos, M., …, Kaushik. (2024). geopandas/geopandas: v0.14.3 (v0.14.3). *Zenodo*. https://doi.org/10.5281/zenodo.10601680

Virtanen, P., Gommers, R., Oliphant, T.E. et al. (2020). SciPy 1.0: fundamental algorithms for scientific computing in Python. *Nat Methods 17*, 261–272. https://doi.org/10.1038/s41592-019-0686-2

Wagner, W., Lemoine, G., & Rott, H. (1999). A Method for Estimating Soil Moisture from ERS Scatterometer and Soil Data. *Remote Sensing of Environment, 70*(2), 191–207. https://doi.org/10.1016/s0034-4257(99)00036-x

Wang, X., Zhang, J., Shahid, S., Guan, E., Wu, Y., Gao, J., & He, R. (2014). Adaptation to climate change impacts on water demand. In Mitigation and Adaptation Strategies for Global Change (Vol. 21, Issue 1, pp. 81–99). Springer Science and Business Media LLC. https://doi.org/10.1007/s11027-014-9571-6

Wickel, A. J., Jackson, T. J., & Wood, E. F. (2001). Multitemporal monitoring of soil moisture with RADARSAT SAR during the 1997 Southern Great Plains hydrology experiment. In International Journal of Remote Sensing (Vol. 22, Issue 8, pp. 1571–1583). Informa UK Limited. https://doi.org/10.1080/01431160120291

Zappa, L., Schlaffer, S., Bauer-Marschallinger, B., Nendel, C., Zimmerman, B., & Dorigo, W. (2021). Detection and Quantification of Irrigation Water Amounts at 500 m Using Sentinel-1 Surface Soil Moisture. In Remote Sensing (Vol. 13, Issue 9, p. 1727). MDPI AG. https://doi.org/10.3390/rs13091727